Advanced Clear-Sky Processor for Oceans (ACSPO)-VIIRS

Algorithm Theoretical Basis Document

Compiled by the

**SST Integrated Product Team (IPT),
NPOESS Data Exploitation Project (NDE),
and Office of Satellite and Product Operations (OSPO)**

Version 1.0

August, 2013

TITLE: ACSPO-VIIRS ALGORITHM THEORETICAL BASIS DOCUMENT

AUTHORS:

Boris Petrenko (GST, Inc.)
John Stroup (STG, Inc.)

DOCUMENT HISTORY
DOCUMENT REVISION LOG

The Document Revision Log identifies the series of revisions to this document since the baseline release. Please refer to the above page for version number information.

DOCUMENT TITLE: Algorithm Theoretical Basis Document Template			
DOCUMENT CHANGE HISTORY			
Revision No.	**Date**	**Revision Originator Project Group**	**CCR Approval # and Date**
1.0	August 2013	Version 1	N/A

LIST OF CHANGES

Significant alterations made to this document are annotated in the List of Changes table.

DOCUMENT TITLE: Algorithm Theoretical Basis Document Template					
LIST OF CHANGE-AFFECTED PAGES/SECTIONS/APPENDICES					
Version Number	**Date**	**Changed By**	**Page**	**Section**	**Description of Change(s)**
1.0	08/28/13	Petrenko	All	All	Original Document

TABLE OF CONTENTS

LIST OF TABLES AND FIGURES

1   INTRODUCTION

Sea surface temperature (SST) is an important environmental variable used in many applications including monitoring of climate variability, seasonal forecasting, operational weather and ocean forecasting, military and defense operations, validating of ocean and atmospheric models, ecosystem assessment, tourism, and fisheries (Donlon et al., 2007). A large part of SST information comes from satellite infrared (IR) instruments, such as Advanced Very High Resolution Radiometer (AVHRR) flown on NOAA and MetOp satellites and Moderate Resolution Imaging Spectroradiometer (MODIS) onboard Aqua and Terra satellites. SST is also one of the key global products from the Visible Infrared Imaging Radiometer Suite (VIIRS) flown onboard the Suomi National Polar-orbiting Partnership (SNPP) satellite since 28 October 2011. The VIIRS will also be onboard the two follow-on Joint Polar Satellite System (JPSS) satellites, J1 and J2, scheduled for launch in 2017 and 2023, respectively.

This document describes the theoretical basis of the global SST L2 product generated from VIIRS with the Advanced Clear-Sky Processor for Oceans (ACSPO). ACSPO is a processing system developed at NOAA STAR with the initial objective to process data of the Advanced Very High Resolution Radiometer (AVHRR) of NOAA satellites for SST, aerosol and clear-sky radiances. Since May 2008, ACSPO has been used for operational processing of the AVHRR data at the NOAA Office of Satellite and Product Operations (OSPO). Since then, the advanced ACSPO versions were being continuously developed, and the scope of ACSPO applications was extended to experimental processing data from all AVHRRs, Aqua and Terra Moderate Resolution Imaging Spectroradiometer (MODIS), and VIIRS (Ignatov et al., 2012; Liang and Ignatov, 2013).

ACSPO has a number of advanced features which make it different from the majority of existing operational SST retrieval systems, such as Pathfinder (Kilpatrick et al., 2001); NASA MODIS (Minnett et al., 2004, Franz, 2009); Interface Data Processing Segment (IDPS – Jackson and Siebels, 2011). These features are as follows:
- ACSPO incorporates the Community Radiative Transfer Model (CRTM – Liang et al., 2009), which performs on-line clear-sky radiative transfer simulations. The inputs for CRTM are the analysis L4 SST and the atmospheric profiles of temperature and humidity from the National Center for Environmental Prediction (NCEP) Global Forecast System. ACSPO allows using the following L4 SST products:
  - Weekly Optimal Interpolation Reynolds SST (Reynolds et al., 2002);
  - AVHRR-based 0.25° Daily High-Resolution-Blended SST (Reynolds et al., 2007), which is currently used operationally;
  - Operational SST and Sea Ice Analysis (OSTIA – Donlon et al., 2012);
  - Canadian Meteorological Centre (CMC) SST (CMC – Brasnett, 1997; 2008)

- The quality the ACSPO SST product is controlled with a special ACSPO module, ACSPO Clear-Sky Mask (ACSM – Petrenko et al., 2010). The ACSM performs downstream of the SST algorithm and detects cloud manifestations directly in the retrieved SST and in deviations of observed brightness temperatures (BT) from ones simulated with CRTM.
- Prior to cloud filtering, the ACSM evaluates global biases in retrieved SST with respect to L4 analysis and in observed BTs with respect to CRTM BTs. Accounting for these biases in the ACSM cloud filters reduces sensitivity of the ACSM to calibration trends and potential biases in retrieved SST (Petrenko et al., 2010).
- Similarly to all other existing operational processing systems, the current ACSPO version 2.2 exploits regression SST algorithms. These algorithms will be periodically upgraded as new and more effective algorithms will be found. In particular, it is planned that the subsequent ACSPO version will incorporate the regression algorithms developed at the EUMETSAT Ocean and Sea Ice Satellite Application Facility (OSI-SAF), which have been shown more efficient than the current ACSPO algorithms (Petrenko et al., 2013a). In addition, availability of CRTM simulations within ACSPO allows using algorithms based on radiative transfer simulations. One of such algorithms, the Hybrid or Incremental Regression (Petrenko et al., 2011), is currently being tested within the experimental version of ACSPO.

1.1   Product overview

1.1.1   Product Description

SST in ACSPO is produced for all clear-sky ocean pixels observed by the VIIRS sensor within full VIIRS swath. Accuracy, precision, computational efficiency and robustness are priorities of the ACSPO SST development.

The general features of the ACSPO SST product are determined by the physics of the transfer of IR radiation in the ocean surface-atmosphere system, as discussed in more detail in section 2.3.1. Since clouds are not transparent for infrared radiation, accurate SST retrieval is possible under clear-sky conditions only. SST estimates in pixels, fully or partially filled with clouds, usually include large negative SST biases. Consequently, the overall quality of the global SST product largely depends on the performance of the product's cloud mask. In addition to the SST estimates, produced in all VIIRS pixels over ocean, the ACSPO SST product includes quality flags, which allow selection of clear-sky pixels. The ACSPO Clear-Sky Mask, which produces the quality flags, is described in section 3.3.2.3.

 In the absence of clouds, the IR radiation coming out of the sea surface is attenuated by the atmospheric water vapor, other atmospheric gases and aerosol. To minimize

atmospheric effects on SST, the SST algorithms use observations in IR bands within the atmospheric transparency windows 8-12 µm (Long Wave Infrared Range - LWIR) and 3.4-4.2 µm (Midwave Infrared Range - MWIR). Furthermore, since the atmospheric absorption varies in different window bands, multichannel retrieval algorithms allow more comprehensive accounting for the atmospheric effects (McMillin et al., 1975). The outgoing radiation in the MWIR transparency window is more sensitive to SST and less affected by the atmospheric absorption than in LWIR bands. However, the MWIR bands cannot be used for SST in the daytime due to contamination with reflected solar radiation. Currently, ACSPO uses regression SST retrieval algorithms (e.g., Petrenko et al., 2010), consistently with all other operational SST systems. These algorithms are the modifications of two approaches developed earlier for AVHRR. The nighttime "Multichannel" SST (MCSST) approach (McClain et al., 1983) exploits both LWIR and MWIR bands. In the case of VIIRS, these bands are M12, M15 and M16 centered at 3.70 µm, 10.76 µm and 12.01 µm respectively. During day, the ACSPO exploits the "Nonlinear" SST (NLSST) approach (Walton et al., 1998) using only LWIR split-window bands M15 and M16 and *a priori* SST T_S^0 which is used as a proxy for atmospheric humidity. The coefficients for the ACSPO SST algorithms are produced from matchups of satellites BTs with *in situ* SST. The ACSPO SST algorithms are described in section 2.3.2.2.

A common problem of regression algorithms is that SST accuracy and precision are sensitive to the atmospheric attenuation and significantly vary in space (Petrenko et al., 2013a). As alternatives to regression, several SST algorithms based on a radiative transfer model (RTM) have been recently developed (Merchant et al., 2009; Le Borgne et al., 2011; Petrenko et al., 2011). These algorithms have been shown capable of providing more uniform SST accuracy and precision than is possible with pure regression. Currently, the one of such algorithms - Incremental Regression - is being tested within the experimental version of ACSPO and it will likely become a baseline SST algorithm in the future operational ACSPO versions.

A frequently asked question about satellite SST is: what ocean layer - "skin" or "bulk" - should it be attributed to? On the one hand, satellite SST is derived from observed brightness temperatures (BTs), which are sensitive to temperature variations in the upper ~10 µm "skin" ocean layer (e.g., Sounders, 1967; Donlon et al., 2002; Minnett, 2003). On the other hand, the regression coefficients are derived from matchups with *in situ* SST measured at ~ 1 m depth ("bulk" SST). The "bulk" SST can differ from "skin" SST due to the skin effect (cold skin layer, due to heat exchange at the surface), and diurnal thermocline (Gentemann et al., 2003; Horrocs et al., 2003; Gentemann and Minnett, 2008). We suggest that satellite SST reflects spatial and temporal variations in "skin" SST, but its absolute value is anchored to "bulk" SST. This problem is discussed in more detail in section 2.3.1.1.

1.1.2 Product Requirements

Table 1-1 shows the requirements to VIIRS SST L2 product as they are formulated in JPSS Program Level 1 Requirements (2013).

EDR attribute	Threshold	Objective
Horizontal cell size	1.6 km[1]	0.25 km
Mapping Uncertainty, 3 sigma	2 km[1]	0.1 km
Measurement Range	271 K to 313 K	271 K to 318 K
Measurement Accuracy[2]	0.2 K	0.05 K
Measurement Precision[2]	0.6 K	0.2 K (<55° View Zenith Angle)
Refresh Rate	12 hrs	2 hrs
Geographic Coverage	Global cloud- and ice-free ocean, excluding lakes and rivers	Global cloud- and ice-free ocean, including large lakes and wide rivers
Notes: 1. Worst case scenarios corresponding to swath edge, both numbers are ~ 1 km at nadir 2. Represent global mean bias and standard deviation validation statistics against quality-controlled drifting buoys (for day and night, and in full VIIRS swath and range of atmospheric conditions). Better performance is expected against ship radiometers.		

Table 1-1. VIIRS SST Requirements

1.2 Satellite Instrument Description

The VIIRS bands have been positioned to optimize their use for SST. The LWIR bands are located in the atmospheric transmission window 8-12 µm near the maximum intensity in Planck's function at temperatures characteristic of the sea surface. There are two suitable regions for selection of LWIR bands for SST: 8-9 µm and 10-13 µm. Three VIIRS LWIR bands are located in these two regions. Figure 1-1 and Figure 1-2 show the radiance at the height of the satellite and the atmospheric transmission for the Thermal IR (TIR) spectrum simulated using the MODTRAN atmospheric radiative transfer code and five standard atmospheres. Bands in the MWIR are located where the atmosphere is transparent and less variable. Figure 1-2 shows that the 3.4-4.2 µm region is a suitable atmospheric window. Two VIIRS MWIR bands are located in this window. The requirement to produce SSTs consistent with those from heritage sensors is also one of the factors for VIIRS band selection. To meet the VIIRS SST measurement requirements, the sensor must have very low radiometric noise in the IR bands. Table 1-2 taken from VIIRS On-orbit performance table (available at https://cs.star.nesdis.noaa.gov/pub/NCC/VIIRS/VIIRS_On-orbitPerformanceTable.pdf) shows the characteristics of VIIRS bands, which are currently

used for SST or can be used in the future. Table 1-2 also shows characteristics of bands M5 and M7, used in the ACSPO Clear-Sky Mask (ACSM).

Band No.	Spectral range (µm)	Horiz Sample Interval (track×scan)		Band Gain	On-Orbit measured SNR or NEdt(K)
		Nadir	End of Scan		
M5	0.662-0.682	0.742-0.259	1.60×1.58	High	321-336.13
				Low	631.26-673
M7	0.846-0.885	0.742-0.259	1.60×1.58	High	435-437.54
				Low	636-631.24
M12	3.660-3.840	0.742-0.776	1.60×1.58	Single	0.13
M13	3.973-4.128	0.742-0.259	1.60×1.58	High	0.04
				Low	
M14	8.400-8.700	0.742-0.776	1.60×1.58	Single	0.06-0.05
M15	10.263-11.263	0.742-0.776	1.60×1.58	Single	0.03
M16	11.538-12.488	0.742-0.776	1.60×1.58	Single	0.03

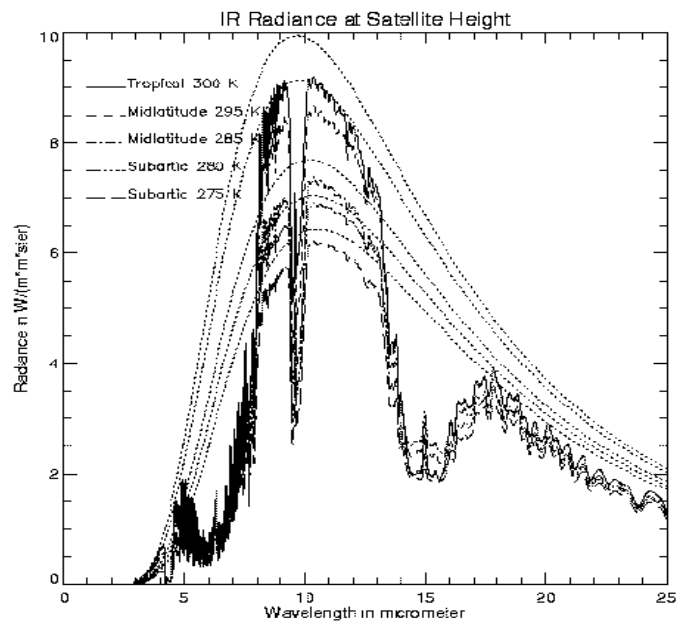*Table 1-2. Channel Characteristics of VIIRS*

Figure 1-1
IR radiance at satellite height for five standard atmospheres simulated by MODTRAN. The
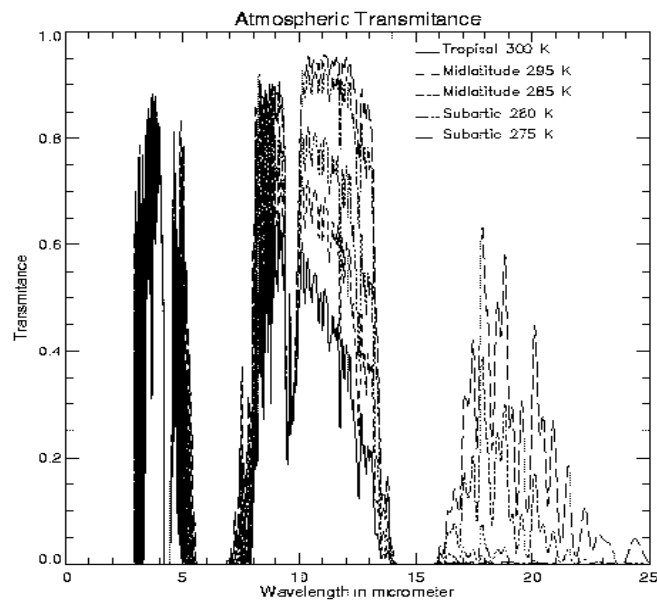*SST at the base of the atmospheres is given in the key in the figure.*

Figure 1-2
As previous figure, but showing atmospheric transmittance.

2 ALGORITHM DESCRIPTION

2.1 Processing Outline

The flow chart of ACSPO is shown in Figure 2-1. The ACSPO processes VIIRS Sensor Data Records (SDR) sequentially in time. The sequence of SDRs is important for accumulation of histograms of deviations of SST from the reference L4 SST and VIIRS BTs from CRTM BTs. The histograms are used in ACSM to estimate global biases in the corresponding variables. If the histogram files are not available at the beginning of processing a given series of SDRs, they are initially calculated from the first processed SDR. The processing of each SDR begins with reading the input data, including analysis L4 SST field and GFS atmospheric profiles which are used as input for CRTM. L4 SST is also used as reference (first guess) SST in SST retrieval. The reference SST field is interpolated from the native grid to sensor's pixels. The simulated clear-sky BTs are also interpolated to all ocean pixels. SST retrievals are performed for all ocean pixels, using two LWIR split-window bands during day and three bands (LWIR and SWIR) during night. The Single Sensor Error Statistics (the estimates of bias and SD of clear-sky SST estimates) in every pixel are produced by interpolation of pre-calculated look-up tables (LUT). The previously accumulated histograms of deviations of retrieved SST from reference SST and observed BTs from CRTM BTs are read from the histograms files and updated using the information from the current SDR. The updated histograms are written in the histogram files, and used to estimate the global biases of the corresponding variables. Finally, the ACSPO Clear-Sky Mask separates clear-sky and cloudy pixels.
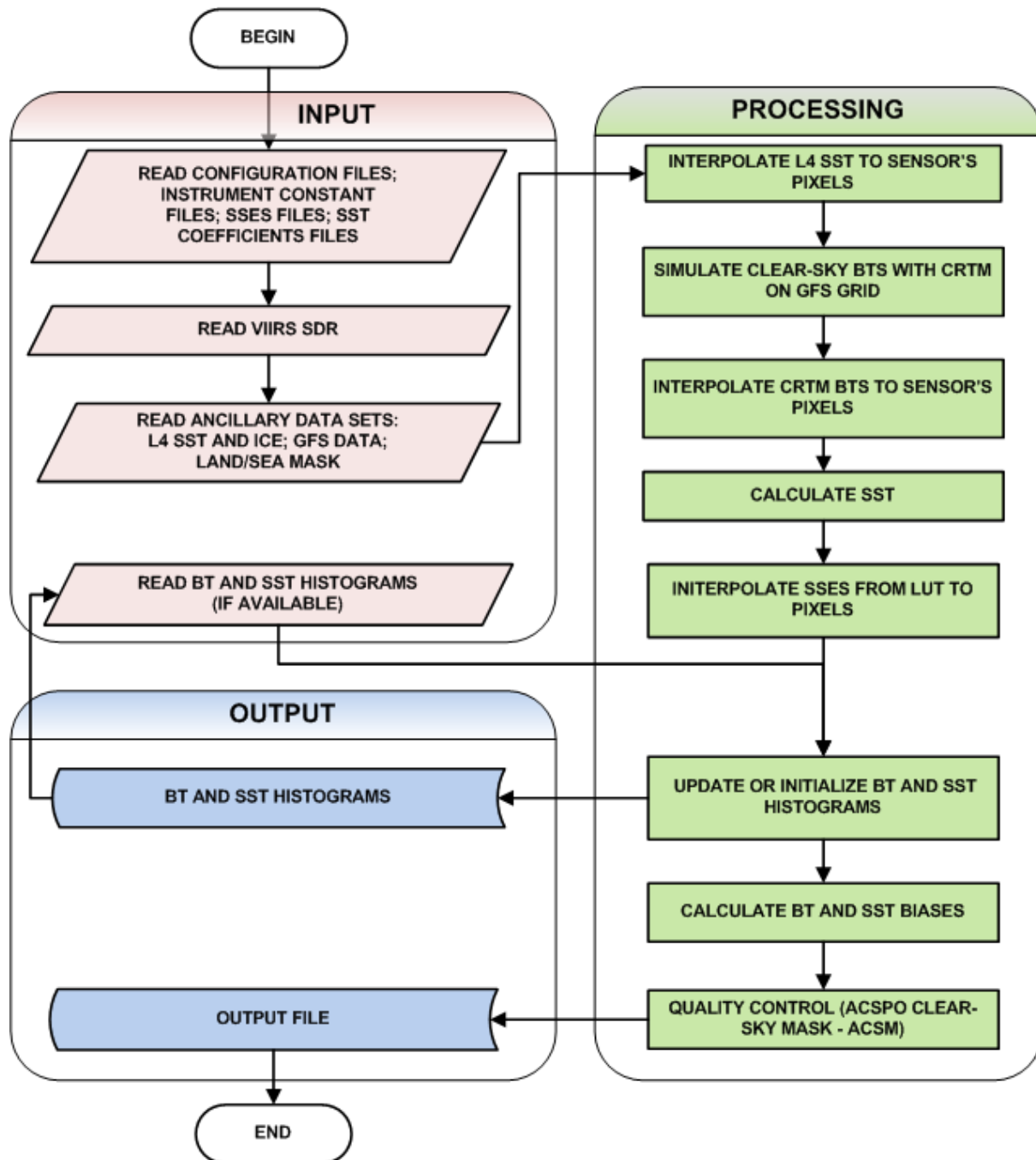
Figure 2-1
The flow chart of ACSPO data processing for SST.

2.2   Algorithm Input

The ACSPO algorithm requires a number of data files to operate properly. These files and various characteristics about them are listed in Table 2-1.

Input Data	Contents	Format	# of Files	Static/ Dynamic
VIIRS moderate resolution radiometric data	Brightness temperatures (BTs) of channels at wavelengths 3.70 μm, 10.76 μm, and 12.01 μm	HDF5	3 (channels M12, M15, M16)	dynamic
VIIRS moderate resolution geo-location data	Latitude, longitude, satellite and solar zenith angles, satellite and solar azimuth angles of radiometric data	HDF5	1	dynamic
Bias correction (optional)	Global deviations of SST from the reference L4 SST and VIIRS BTs from CRTM BTs	ASCII	4 (one for each channel and one for SST)	dynamic
L4 reference SST data	Gridded daily SST and sea ice concentration	NetCDF4	1	dynamic
Forecast model data	Meteorological fields used for simulation of clear-sky radiances by the Community Radiative Transfer Model (CRTM)	HDF4	2	dynamic
Instrument constants	Instrument-specific constants	ASCII	1	static
Algorithm constants	SST regression coefficients	ACSII	1	static
SSES LUT	SST bias and standard deviation as functions of view zenith angle and total precipitable water vapor content in the atmosphere	ASCII	1	static
CRTM coefficients	Transmittance, spectral, cloud, aerosol, and emissivity coefficient data needed by the CRTM	binary	13	static
Surface properties	Land/sea mask, bathymetry, and land/water distances	HDF4	1	static

Table 2-1. ACSPO Input Data

2.3 Theoretical description

2.3.1 Physical description

2.3.1.1 Skin and bulk SST

Surface IR emission is formed in the top ~10 μm of water and is sensitive to the so-called "skin" SST (e.g., Sounders, 1967; Donlon et al., 2002; Minnett, 2003). *In situ* sensors, on the other hand, typically measure "bulk" SST, which differs from "skin" SST due to the skin effect (cold skin-layer, due to heat exchange at the surface), and diurnal thermocline (e.g., Gentemann et al., 2003; Horrocks et al., 2003; Gentemann and Minnett, 2008). The difference between skin and bulk SSTs may reach several degrees, especially during the daytime under clear-sky and low wind conditions, when the mixing in the upper layer is suppressed and therefore strong diurnal warming may develop (Fairall, 1996; Murray et al., 2000; Wick et al., 2002; Castro et al., 2002; Stuart-Menteth et al., 2003; Tanashi et al., 2003; Nardielli et al., 2005). Figure 2-2 shows typical vertical distributions of SST during day and night, and gives definitions of SSTs. Using *in situ* bulk SSTs for validation of the skin SST product has limitations. Existing approaches to nighttime skin-to-bulk SST conversion may use a constant offset of ~0.17 K. If surface wind speed, w, is available, then the following relationship between skin and bulk SST was proposed by Donlon et al (2002):

$$SST_{bulk} = SST_{skin} - [0.14 + 0.30\exp(-w/3.7)] \qquad (2.1)$$

During daytime, the relationship between skin and bulk SSTs is more complex, due to the effect of the diurnal thermocline. Its modeling requires knowledge of fluxes at the surface, including their history. In this ATBD, correction of *in situ* data and retrieved SST for skin/bulk difference was not applied. The coefficients for regression and hybrid algorithm were calculated from matchups of BTs and *in situ* bulk SSTs. On the other hand, the observed BTs, from which the SST products are derived, are sensitive to skin SST. As a result, retrieved SST reflects variations in skin SST, but on average represents bulk SST.

2.3.1.2 Surface emissivity

Ocean surface is not a black body. Overall, emissivity of sea water is well constrained (compared to, e.g., land emissivity). It is less than unity and depends upon spectral interval and view angle (e.g., Smith et al., 1996; Watts et al., 1996). Spectral and angular structure of emissivity is defined by Fresnel's laws and sea surface roughness. Typical emissivities of a flat surface in the thermal IR windows representative of AVHRR bands 3b, 4 and 5 or the corresponding VIIRS bands M12, M15 and M16 are shown in Figure 2-2. They were calculated with spectral refractive indexes (Friedman, 1969; Hale and Querry, 1973; Downing and Williams, 1975; Pinkley et al., 1977; Segelstein, 1981).
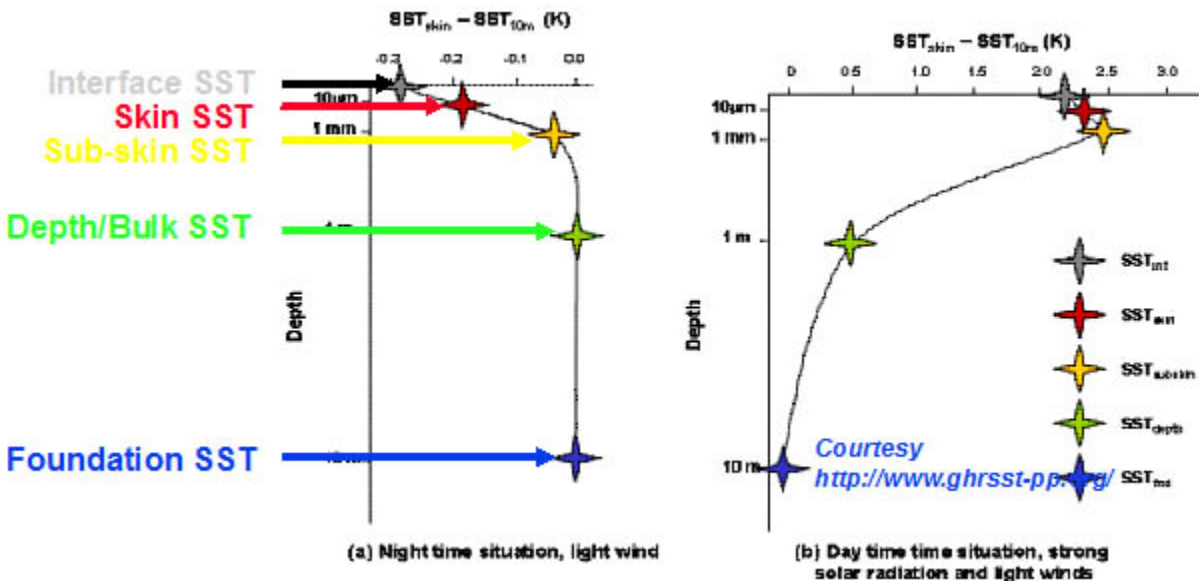
Figure 2-2
Definitions of different SSTs (after Donlon et al., 2007):
Interface SST is a temperature at exact air-sea interface
Skin SST is a temperature measured by IR radiometer at ~10-20µm depth
Subskin SST is a temperature at the base of a conductive laminar sub-layer
Depth/bulk SST is a temperature measured by drifting buoys at ~1 m depth
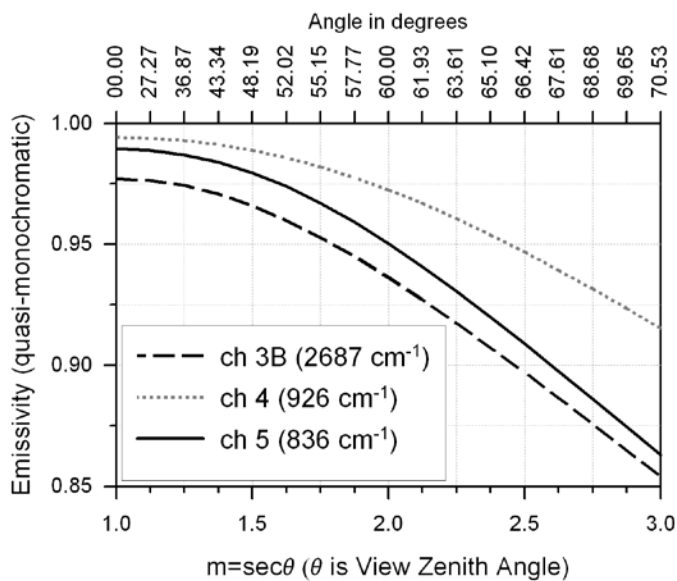*Foundation SST is a temperature of the water column free from diurnal variability*

Figure 2-3
Typical spectral and angular dependence of sea water emissivity in the AVHRR bands
(Dash and Ignatov, 2008).

Emissivity is also a function of wind speed (e.g., Wu and Smith, 1997; Minnett et al., 2001; Masuda et al., 2006), water temperature, and salinity (e.g., Newman et al., 2005). These corrections are relatively small but can introduce errors in SST retrievals up to several tenths of a degree Kelvin (e.g., Hanafin and Minnett, 2005; Niclos et al., 2005; Donlon et al., 1998, 2002).

2.3.1.3 Atmospheric transmittance

Assuming clear sky conditions and neglecting atmospheric scattering, the top of atmosphere (TOA) radiance (I(v)) is customarily described by (e.g., Dash and Ignatov, 2008)

$$I(v) = I_s(v) + I_{atm}(v)^{\uparrow} + I_{atm}(v)^{\downarrow} \qquad (2.2)$$

Here, $I_s(v)$, $I_{atm}(v)^{\uparrow}$ and $I_{atm}(v)^{\downarrow}$ represent the surface emission, atmospheric upwelling, and reflected downwelling radiance, respectively, and v is frequency.

Satellite SST retrievals are performed in infrared (IR) bands where the surface emission reaches its maximum, yet atmospheric absorption is small (c.f. Figure 1-1 and Figure 1-2). Atmospheric transmittance varies depending upon atmospheric conditions and in the atmospheric windows is mostly defined by water vapor and temperature profiles (e.g., Saunders, 1967; Prabhakara et al., 1974; McMillin, 1975; Llewellyn-Jones et al., 1984). Typically, atmospheric correction algorithms are aimed at minimizing the water-vapor-induced error in retrieved SST. Minor gases also affect transmission in the window bands, but their effect is typically small and much less variable in space and time (e.g., Dash and Ignatov, 2008).

Under typical maritime conditions, aerosol effects on atmospheric transmission in the window regions are smaller than the water vapor effects (e.g., Dash and Ignatov, 2008). These effects are much more complex and less explored (e.g., Walton, 1985; Walton et al, 1998; Merchant and Harris, 1999; Highwood et al., 2003; Vazquez et al., 2004; Hollweg et al., 2006; Nalli and Reynolds, 2006; Castro et al., 2008). Empirical correction for the effects of aerosols have been explored in the past (e.g., Nalli and Stowe, 2002; Merchant et al., 2006) but they remain limited in scope. A more appropriate way to perform aerosol correction is based on an approach consistent with physical SST retrievals, i.e., using RTM with a global first-guess aerosol field (e.g., the Goddard Chemistry Aerosol radiation and Transport, or GOCART, Chin et al., 2000; the Navy Aerosol Analysis and Prediction System, or NAAPS, found at www.nrlmry.navy.mil/aerosol/). This approach appears relatively straightforward, at least in principle. However, it requires substantial investment in CRTM improvement and GOCART data exploration and may be explored later beyond the 100% ATBD.

Another factor that affects the top-of-atmosphere radiances is residual and ambient cloud. Effect of this factor on SST may be significant but it is even less explored than aerosols (e.g., Vazquez et al., 2004; Dash and Ignatov, 2008; Liang et al., 2009).

During daytime, the shortwave IR window is subject to solar reflection and scattering. Unless these signals are corrected for, the shortwave band cannot be used during the day. Solar reflectance and scattering is also present in the longwave bands too, but the corresponding signals are much smaller there. However, the effect may reach from several tenths to several degrees of Kelvin in the glint areas (e.g., Khattak et al., 1991; Nath et al, 1993). Correcting for this effect or screening data in the glint area is thus needed for accurate SST retrievals during daytime.

In IR bands, each of the components in Eq. (2.2) can be expressed mathematically as follows

$$I_s(v) = \varepsilon(v)\tau_0(v)B(v,T_s) \tag{2.2a}$$

$$I_{atm}(v)^{\uparrow} = \int_z^0 B(v,T_p(z))\frac{\partial\tau(v,z)}{\partial z}dz \tag{2.2b}$$

$$I_{atm}(v)^{\downarrow} = (1-\varepsilon(v))\tau_0(v)\int_0^z B(v,T_p(z))\frac{\partial\tau(v,z)}{\partial z}dz \tag{2.2c}$$

(Note that each term in equation 2.2 is view angle dependent but this dependence was omitted here for simplicity.) Here, ε is the surface emissivity, τ is the atmospheric transmittance, τ_0 is the atmospheric transmittance from the surface to the top of the atmosphere, z is the height, T_s is the surface temperature;, $B(v,T_s)$ is the Planck function, and $T_P(z)$ is a temperature profile in the atmosphere. The equations (2.2) describe radiative transfer in the atmosphere in the absence of scattering. Atmospheric scattering should be taken into account in the 3.9-μm band during daytime, and the scattering term should be added to equation 2.2b. However, the CRTM currently does not take into account scattering. Hence, at this writing, shortwave bands are not used for SST in the daytime, and the scattering term in (2.2b) is neglected.

2.3.2 Mathematical Description

2.3.2.1 Simulation of clear-sky brightness temperatures and interpolation of gridded auxiliary data to sensor's pixels

The Community Radiative Transfer Model (CRTM, Han et al., 2006; Chen et al., 2012a, 2012b) is employed in ACSPO to simulate top of atmosphere clear-sky BTs, using the GFS atmospheric profiles of temperature and humidity and L4 SST fields as inputs (Liang et al., 2009, Liang and Ignatov, 2011). CRTM BTs are computed on the GFS grid. Along with clear-sky BTs, BT derivatives in terms of SST are also calculated. Both BTs and their derivatives are then interpolated to the sensor's pixels. Similar interpolation is applied to selected GFS variables, such as TPW. The pixel-level first guess SST is produced by spatial interpolation of the gridded analysis SST.

2.3.2.2 Regression SST algorithms

The expressions (2.3) and (2.4) demonstrate the regression SST algorithms currently used in ACSPO during respectively day and night. These equations were suggested by Lavanant et al. (2012) for processing VIIRS data based on the experience of processing Metop-A AVHRR data at the EUMETSAT Ocean and Sea Ice Satellite Application Facility (OSI-SAF Low Earth Orbiter Sea Surface Temperature Product User Manual, Version 2.1, 2009). The peculiarity of equations (2.3, 2.4) is that they emphasize the dependency of regression coefficients on VZA. The comparisons of existing operational SST algorithms (Petrenko et al., 2013a) has confirmed a high efficiency of this approach for processing VIIRS data within a full swath, i.e., within a full range of VZAs. The nonlinear SST algorithm (NLSST) does not use the 3.9 μm band:

$$T_S = a_0 + (a_1 + a_2\, S_\theta)\, T_{11} + [a_3 + a_4\, (T_s^0 - 273.15) + a_5\, S_\theta]\, (T_{11} - T_{12}) + a_6 S_\theta \quad (2.3)$$

The multi-channel SST algorithm (MCSST) uses the 3.9-μm band and is applicable only in the nighttime, when this band is not contaminated by sunlight scattering and reflection:

$$T_S = a_0 + (a_1 + a_2\, S_\theta)\, T_{3.7} + (a_3 + a_4 S_\theta)\, \Delta T_{11\text{-}12} + a_5 S_\theta \quad (2.4)$$

In (2.3) and (2.4), T_S is regression SST estimate, T_4, T_{11} and T_{12} are brightness temperatures (BT) in M12, M15 and M16 (3.7, 10.8 and 12 μm) bands, T_s^0 is first guess (*a priori*) SST, $S_\theta = sec(\theta)-1$, θ is VZA, and *a*'s are regression coefficients computed from matchups of *in situ* SST T_{IS} with observed BTs. All temperature values are in Kelvin.

The regression coefficients for VIIRS SST (*a*'s) are derived from dataset of matchups (MDS) of VIIRS BTs against *in situ* SST. The currently used (as for October 2013) coefficients for VIIRS were obtained from matchups, collected from 16 October 2012 to 15 October 2013. The MDS includes matchups of VIIRS BTs in bands M12 (3.7 μm), M15 (10.8 μm), and M16 (12 μm) with drifters' SSTs from the *In situ* Quality Monitor (*i*Quam; Xu and Ignatov, 2010, 2013, available at www.star.nesdis.noaa.gov/sod/sst/iquam/). Satellite L1b data were processed with the ACSPO. The ACSPO Clear-Sky Mask (ACSM) (Petrenko et al., 2010) was used to select clear-sky matchups. The time interval between in situ and satellite measurements is ≤ 2hrs, and the distances between the buoy locations

and the nearest clear-sky pixel are ≤ 10 km. The current coefficients for equations (2.3) and (2.4) are given in Table 2.2.

Table 2.2. Coefficients for regression equations (2.3) and (2.4).

Equation	a_0	a_1	a_2	a_3	a_4	a_5	a_6
Day (2.3)	5.623045	0.985192	0.019775	0.456758	0.067732	0.705117	-4.714369
Night (2.4)	0.236653	1.003204	0.032301	0.992169	0.241534	-8.055822	N/A

2.3.2.3 ACSPO Clear-Sky Mask (ACSM)

2.3.2.3.1 The concept and the structure of ACSM

Typically, only about 15-20% of ocean pixels are cloud-free to the extent that they are usable for SST retrieval from thermal IR measurements. Therefore, effective cloud masking is critically important for the quality of SST product. In ACSPO, the cloud masking is performed by the Clear-Sky Mask (ACSM), which performs downstream the SST algorithm. Note that SST in ACSPO is retrieved in <u>all</u> ocean pixels <u>prior to</u> ACSM.

The main concept of ACSM is testing retrieved SST T_S and observed BTs T_B for consistency with the reference SST T_S^0 and CRTM BTs T_B^{CRTM} (Petrenko et al., 2010), and, consequently, the basic cloud predictors in ACSM are SST and BT increments:

$$\Delta T_S = T_S - T_S^0 \tag{2.5a}$$

and

$$\Delta T_B = T_B - T^{CRTM} \tag{2.5b}$$

The ACSM modifies ΔT_S by subtracting the global bias B_{SST}, estimated from the accumulated histogram, this way producing the de-biased SST increment:

$$\Delta T_S^* = \Delta T_S - B_{SST} \tag{2.6a}$$

The BT increment is also modified in ACSM by accounting for the corresponding estimated bias and the difference between T_S and T_S^0 (i.e., non-zero SST increment):

$$\Delta T_B^* = \Delta T_B - G\Delta T_S^* - B_{BT} \tag{2.6b}$$

In (2.6b), G is the derivative of T^{CRTM} in terms of SST, calculated with CRTM.

ACSM also uses predictors constructed from reflectances measured in the optical VIIRS bands M5 (0.672 µm) and M7 (0.865 µm). The filters exploiting reflectance bands are used in the daytime only.

The ACSM classifies ocean pixels into three categories: "Clear," "Probably Clear" and "Cloudy". The ACSM is classified "Cloudy" if it fails at least one of the following five filters:

1. <u>Static SST filter</u>

2. <u>Adaptive SST filter</u>

3. <u>Brightness Temperature filter (BTF)</u>

4. <u>Reflectance Gross Contrast filter</u> <u>(RGCF)</u> (daytime only)

5. <u>Reflectance Relative Contrast filter</u> <u>(RRCF)</u> (daytime only).

Once the ocean pixels have been classified into "Clear" and "Cloudy" categories the two following texture filters reclassify some of "Clear" pixels into "Probably Clear" category:

6. <u>Uniformity filter</u>

7. <u>SST/Reflectance Cross-Correlation filter (CC) (daytime only)</u>

Eventually, the pixel is classified "Clear" if it has passed all the filters listed above.

2.3.2.3.2 SST and BT bias estimation within ACSPO

Figure 2-4 shows global biases between BTs, simulated with CRTM (T_B^{CRTM}) and observed BTs (T_B) observed at 11 µm band of several high-resolution satellite radiometers including VIIRS. The biases were estimated on a daily basis by averaging over clear-sky pixels identified by the ACSM. The biases reach ~0.9K (~0.5 K for VIIRS) and vary in time and between different instruments. This may be due to inaccurate input data for CRTM or incomplete (i.e., missing aerosol attenuation) or not fully accurate CRTM (e.g., Liang et al., 2009). Retrieved SST T_S can be biased too with respect to first guess analysis SST T_S^0 (which is typically anchored to *in situ* SST, e.g., Reynolds et al., 2007) because of inaccurate regression coefficients. BT and SST biases may vary in time due to sensor calibration trends and orbital drift. If these biases are not accounted for, they affect the output of ACSM, which uses SST and BT increments as input for cloud filters.
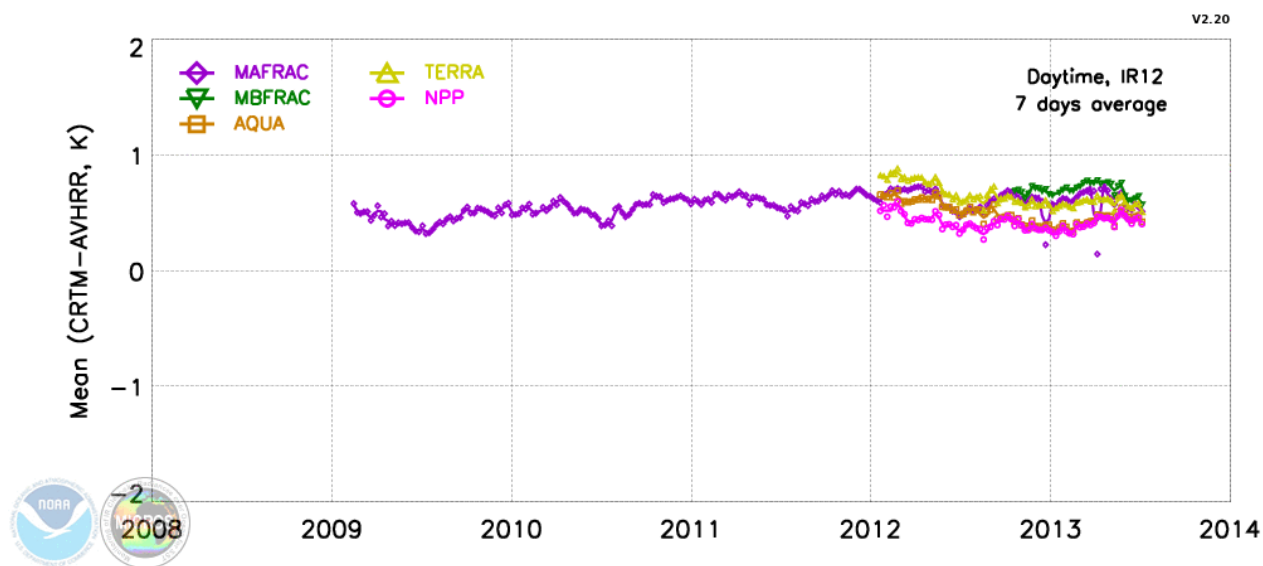
Figure 2-4

Time series of global biases of simulated BT minus observed BT in 11 μm band of MetOp-A AVHRR (MAFRAC), MetOp-B AVHRR (MBFRAC), MODIS-Aqua, MODIS-Terra and JPSS VIIRS (NPP) (from http://www.star.nesdis.noaa.gov/sod/sst/micros/)

In order to reduce the sensitivity of ACSM to SST and BT biases, B_S and B_{BT}, the ACSM corrects the corresponding increments, ΔT_S and ΔT_B, for estimated biases, as shown in (2.6a-b).

The most straightforward method to estimate B_{SST} and B_{BT} is to average ΔT_S and ΔT_B over the pixels indentified by ACSM as "clear-sky" (e.g., Liang et al., 2009). However, if the biases estimated this way are used in ACSM, this may create an undesirable crosstalk between the ACSM pixel classification and bias estimates. Therefore, ACSM uses an alternative bias estimation method, which does not rely on the pixel classification. The biases are estimated as positions of peaks of ΔT_S and ΔT_B histograms, accumulated over ocean, without separating pixels into "clear" and "cloudy". This is done prior to all cloud fitlers listed in Section 2.3.2.3.1. Though the percentage of "clear-sky" ocean pixels is typically only ~15%, the clear-sky values of ΔT_S and ΔT_B are concentrated in a relatively narrow range and form peaks of all-sea-pixels histograms. ACSPO processes VIIRS SDRs sequentially, and the all-sea-pixels histograms are updated recursively for every new SDR:

$$H_1 = S_1 \tag{2.7}$$

$$H_i = \gamma H_{i-1} + S_i, \ i>0, \tag{2.8}$$

$$\gamma = 0.1**(N^{scans}*T^{scan}/\delta/3600) \tag{2.9}$$

Here S_i(i=1,2,…) is the histogram, accumulated from the ith SDR only; H_i is a recursively updated histogram after processing the ith segment. N^{scans} is a number of scans within every SDR, T^{scan} is the time taken by a single instrument scan. Note that the VIIRS instrument includes 16 detectors which perform 16 scans simultaneously for 1.7778 sec. Therefore, the average time talken by one VIIRS scan is T^{scan} = 1.7778/16=.1111125 sec. The coefficient γ is calculated from (2.9) in such a way that the relative contribution of a given segment to H_i reduces in time, so that for δ hours-old segment this relative contribution is approximately 0.1. The parameter δ, palying a role of the integration time, set to 12 hours. Since daytime and nighttime T_S are produced with different algorithms (NLSST and MCSST respectively), and SST is subject to diurnal variability, the SST and BT histograms are accumulated separately for day and night.

Figure 2-5 shows the examples of time series of biases in ΔT_S, retrieved with the nighttime algorithm (2.4) estimated by averaging ΔT_S over clear-sky pixels for a given orbit and from the location of the peak of all-sea-pixel histogram for four NOAA AVHRRs. The two bias estimates are consistent with standard deviation 0.09 K, while the biases vary between the platforms from -1.02 K for NOAA 16 to -0.14 K for Metop-A.
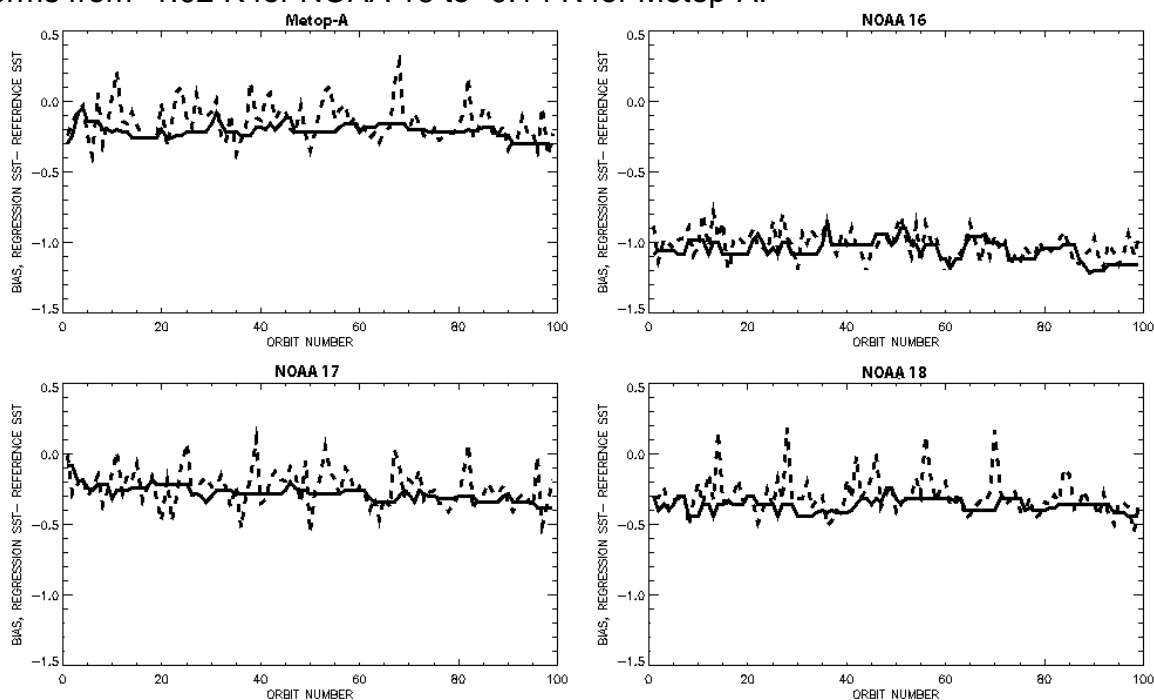

Figure 2-5
Time series of nighttime SST biases for 100 orbits of each of four AVHRRs, August 1–7 2008. Solid lines represent the biases, estimated as locations of peaks of the SST anomaly histograms, accumulated over all sea pixels. Dashed lines represent the biases, estimated as average SST anomaly over "clear" pixels.

2.3.2.3.3 ACSM Filters

2.3.2.3.3.1 Static SST test

The Static and Adaptive SST filters in the ACSM can be viewed as two parts of a single SST filter because the Adaptive SST filter uses as the first guess the pixel classification by the Static SST filter. However, here we will follow the traditional approach, in which these filters are considered separately (Petrenko et al., 2010; Ignatov et al., 2010; Petrenko et al., 2013c).

The predictor for the static SST test is de-biased SST increment $\Delta T_S{}^*$ defined in (2.6a). The test cuts off large negative values of ΔT_S by comparing them against the threshold μ:

$$\Delta T_S > \mu ? \tag{2.10}$$

If yes, then the pixel is set to "Clear;" otherwise, it is set to "Cloudy."

The value of μ is selected to provide a reasonable trade-off between rejecting pixels contaminated with clouds and detecting true cold SST increments in clear-sky areas. In ACSPO v.2.2, μ depends on spatial variability of the BT difference δT between the VIIRS bands M15 and M16 during day and bands M12 and M15 at night:

$$\text{Day:} \quad \delta T = T_{11} - T_{12} \tag{2.11a}$$

$$\text{Night:} \; \delta T = T_{3.7} - T_{12} \tag{2.11b}$$

Higher spatial variability of δT is in general associated with higher probability of clouds in the observed area. However, the spatial variability of δT can also increase in clear-sky dynamic areas due to thermal fronts on the ocean surface. In order to reduce the effect of ocean fronts on δT, it is modified by subtracting median of δT, calculated within 3×3 spatial window centered at a tested pixel:

$$\delta T^* = \delta T - median(\delta T), \tag{2.12}$$

and the variance of δT^* is defined as

$$Var(\delta T^*) = <(\delta T^* - <\delta T^*>)^2> \tag{2.13}$$

Here, $<^*>$ denotes averaging over a 41×41 spatial window centered at a tested pixel. The size of this window for VIIRS was set from empirical considerations. The value of the threshold μ in (3.10) is set depending on $Var(\delta T^*)$ as follows:

$$\text{If } Var(\delta T^*) < \varepsilon \qquad \text{than } \mu = -2 \text{ K}, \text{ otherwise } \mu = -4 \text{ K}, \tag{2.14}$$

ε=0.06 K during day and 0.08 K during night.

2.3.2.3.3.2 Adaptive SST filter

The Static SST filter initially classifies the pixel into "Clear" and "Cloudy" by detecting large negative SST increments exceeding μ, according to (2.10). However, usually these significant cloud manifestations are surrounded with "ambient" clouds, whose effect on SST is small enough to be detected with the Static SST filter. The purpose of the adaptive SST filter is to detect the effects of ambient cloudiness in the neighborhood of clusters of "Cloudy" pixels detected by the condition (2.10). It applies to all pixels, classified "Clear" by the Static SST filter and analyzes the statistics of "Cloudy" pixels within the sliding windows surrounding the tested pixels. The size of the sliding window for VIIRS was empirically set to 41×41 pixels.

Within each sliding window, the test extracts the cluster of "Cloudy" pixels and determines mean SST increment ΔT_{CLD} and its standard deviation (SD) σ_{CLD} over this cluster. Then, for all "Clear" pixels within the window, it calculates the "statistical distance" ρ_{CLD} of ΔT_S from ΔT_{CLD}:

$$\rho_{CLD} = |\Delta T_S - \Delta T_{CLD}|/\sigma_{CLD}. \tag{2.15}$$

Similarly, the statistical distances from the reference SST are determined for all "Clear" pixels as follows:

$$\rho_{CLR} = |\Delta T_S|/\sigma_{CLR,} \tag{2.16}$$

Here, $\sigma_{CLR} = |\mu|/3$. The two statistical distances, ρ_{CLD} and ρ_{CLR}, are compared foe all "Clear" pixels, and those pixels, for which

$$\rho_{CLD} < \rho_{CLR,} \tag{2.17}$$

are added to the "Cloudy" cluster. If this addition changes ΔT_{CLD} and σ_{CLD}, these statistics are recalculated, and all the pixels still belonging to the "Clear" cluster are tested again for the condition (3.17). This iterative process can end by fulfillment of one out of three following conditions:
  1) The condition (2.17) is met for the tested pixel (i.e. the central pixel in the sliding window).
  2) No new pixels have been included in the "Cloudy" cluster at a certain iteration;
  3) A predefined number of iterations has exceed the predefined number N (N=3 in ACSPO v.2.2).
In the case 1) the tested pixel is reclassified as "Cloudy". In the cases 2 and 3 it remains "Clear".

The performance of the static and the adaptive SST filters is illustrated in Figure 2-6. Figure 2-6a shows the nighttime image of $\delta T = T_{3.7} - T_{12}$ by nighttime VIIRS observations on 6

October 2012, Figure 2-6b shows the image of SST increment $T_S - T_S^0$ produced without bias correction and cloud mask. A certain correlation of δT and $T_S - T_S^0$ is noticeable in the central parts of Figure 2-6, a and b. Figure 2-6c is the image of $\text{Var}(\delta T^*)$, calculated according (2.12) and (2.13). The values of $\text{Var}(\delta T^*)$ are uncorrelated with $T_S - T_S^0$ and clearly separate the image into two parts, out of which the smaller values indicate the area with lower probability of clouds, and lager values correspond to areas with higher cloud probability. Figure 2-6d demonstrates the image of $T_S - T_S^0$ with the imposed cloud mask. Setting the lower threshold $\mu = -4$ K for the first area allows detection of large cold SST increments in the central part of Figure 2-6d, whereas higher values of $\mu = -2$ K provide more conservative cloud screening in the areas with larger $\text{Var}(\delta T^*)$ values.

Figure 2-7 demonstrates the images of SST increments, $T_S - T_S^0$ (without bias correction) with the cloud mask produced by sequential application of the Static SST filter and the Adaptive SST filter to SST increments produced from daytime MetOp-A AVHRR observations over the Mexican Gulf on 3 February 2013. The Static SST filter produces a relatively liberal cloud mask, which allows multiple cloud leakages (Figure 2-7a). The Adaptive SST filter makes the cloud mask more conservative by filtering out most of residual clouds (Figure 2-7b).

2.3.2.3.3.3 BT filter

The BTF verifies accuracy of fitting observed BTs, T_B, with BTs simulated with CRTM, T^{CRTM}. Since T^{CRTM} are calculated for clear-sky atmosphere, the absolute difference between T_B and T^{CRTM} usually increases in the presence of clouds. The inputs for the BT test are de-biased BT increments ΔT_B, corrected for ΔT_S, according to (2.6b). In the ACSPO versions preceding v.2.2, the BTF condition was formulated as follows:

$$\Phi_{BT} < \beta ? \tag{2.18}$$

If "Yes" then the pixel is "Cloudy", otherwise it's "Clear". The threshold $\beta = 1.025$, the function Φ_{BT} is calculated as follows:

$$\text{Day:} \quad \Phi_{BT} = ((\Delta T_{B11}^*)^2 + (\Delta T_{B12}^*)^2)/2, \tag{2.19a}$$

$$\text{Night:} \quad \Phi_{BT} = ((\Delta T_{B11}^*)^2 + (\Delta T_{B12}^*)^2 + (\Delta T_{B3.7}^*)^2)/3, \tag{2.19b}$$

ΔT_{B11}^*, ΔT_{B12}^* and $\Delta T_{B3.7}^*$ are de-biased BT increments in bands M15, M16 and M12 respectively, calculated according (2.6b). Initially, the filter (2.18) was created to shape the quasi-gaussian form of the histograms of BT increments without significant effect on the statistics of SST increments. Later, the closer consideration of the BTF effects on SST has shown that this filter causes multiple false cloud detections in the tropical regions due to abnormal distributions of the water vapor in the atmosphere. While these events are successfully handled by the SST algorithm, they cause abnormally large BT increments,

which do not pass the condition (2.18). Therefore, in the ACSPO version 2.2, the BTF is used in two different formulations. The formulation (2.18-2.19) is still used to shape the quasi-gaussian histogram of BT increments in MICROS, and the new and more relaxed formulation of BTF is used for SST. According to this new formulation, the pixel is classified as "Clear" if the following condition is met:

$$a_{11}(\Delta T_{B11})^2 + a_{22}(\Delta T_{B12})^2 + 2a_{12}\Delta T_{B11}\Delta T_{B12} < \gamma/k(\Delta T_S^*), \qquad (2.20)$$

Otherwise the pixel is classified as "Cloudy". In (3.20), $a_{11}=101.0$, $a_{22}=70.15$, $a_{12}=82.49$. The values of γ are tabulated in the LUT as function of VZA and TPW and interpolated from LUT to pixel values of VZA and TPW. Typically, $\gamma=30$ at low atmospheric absorption and grows to 100 for VZA >65° and TPW >5 g/cm^2. The coefficient $k(\Delta T_S)$ accounts for the assumption that the probability of clouds is higher when ΔT_S is significantly negative and it is lower when ΔT_S is significantly positive:

$$k(\Delta T_S) = 1 \text{ if } \Delta T_S > 0.5 \text{ K} \qquad (2.21)$$
$$k(\Delta T_S) = 2 \text{ if } \Delta T_S < -0.5 \text{ K},$$

If $-0.5K \leq T_S \leq 0.5$ K then $k(\Delta T_S)$ is linearly interpolated between 1 and 2.

Figure 2-8 compares the cloud masks produced with ACSPO v.2.02, using the BTF formulation (2.18) and with ACSPO v.2.2, using for SST the formulation (2.20). The latter ACSPO version reveals a remarkable number of previously hidden "Clear" pixels with near-zero or even positive SST increments. Figure 2-9 shows the reflectance in the VIIRS band M7 for the same scene. Comparison of Figure 2-8 and Figure 2-9 shows that the reflectance of pixels revealed with ACSPO v. 2.2 is mainly low, which suggests high probability of those pixels being "clear".
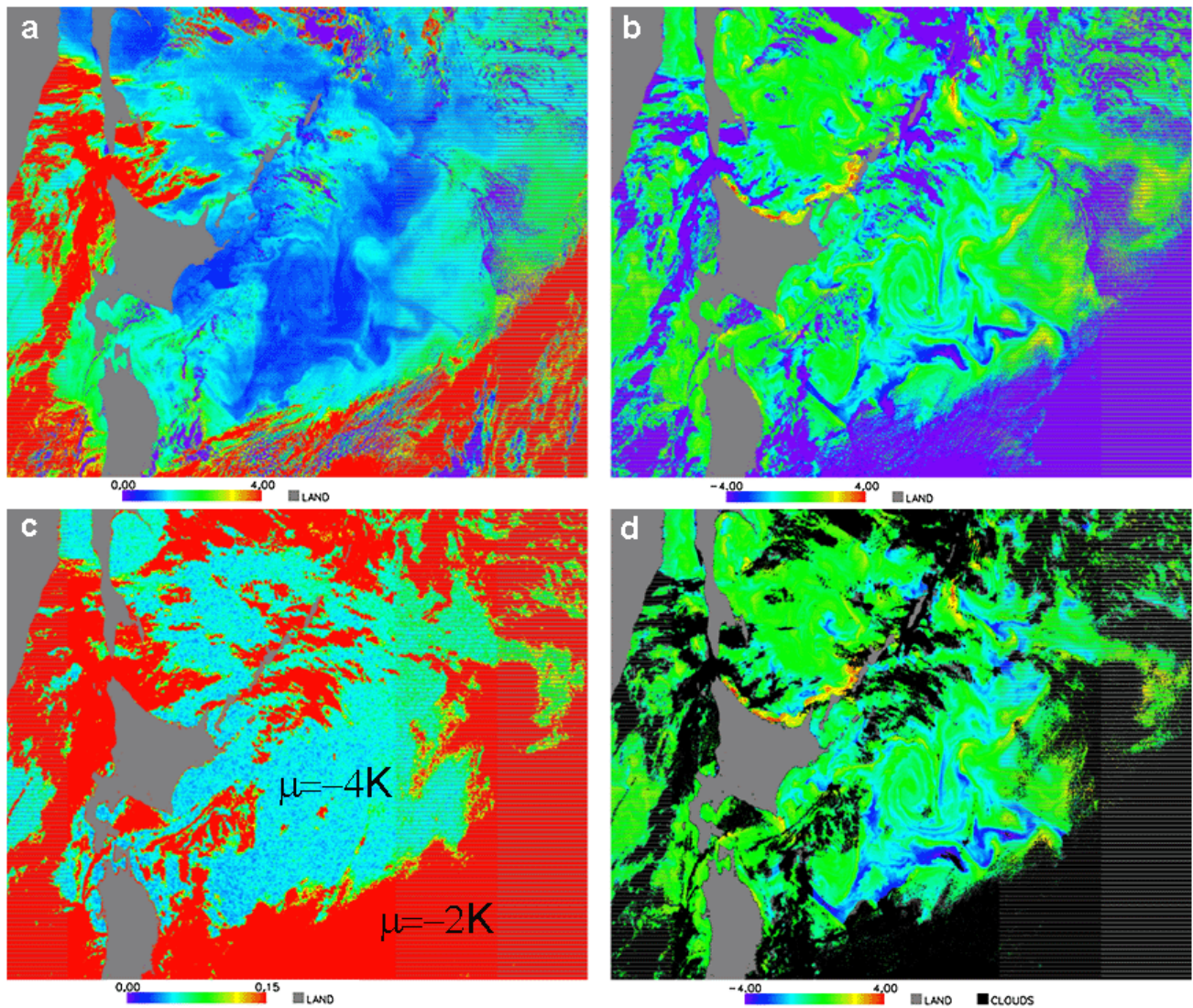
Figure 2-6
The example of selection of the static threshold μ and the image of ΔT_S from the nighttime VIIRS observations from VIIRS over Pacific Ocean near Japan on 6 October 2012. a) the images of BT difference, $\delta T = T_{3.7}-T_{12}$; b) the image of the SST increment, T_S-T_0, without cloud mask; c) the image of Var(δT^*); d) the image of the SST increment with cloud mask imposed.
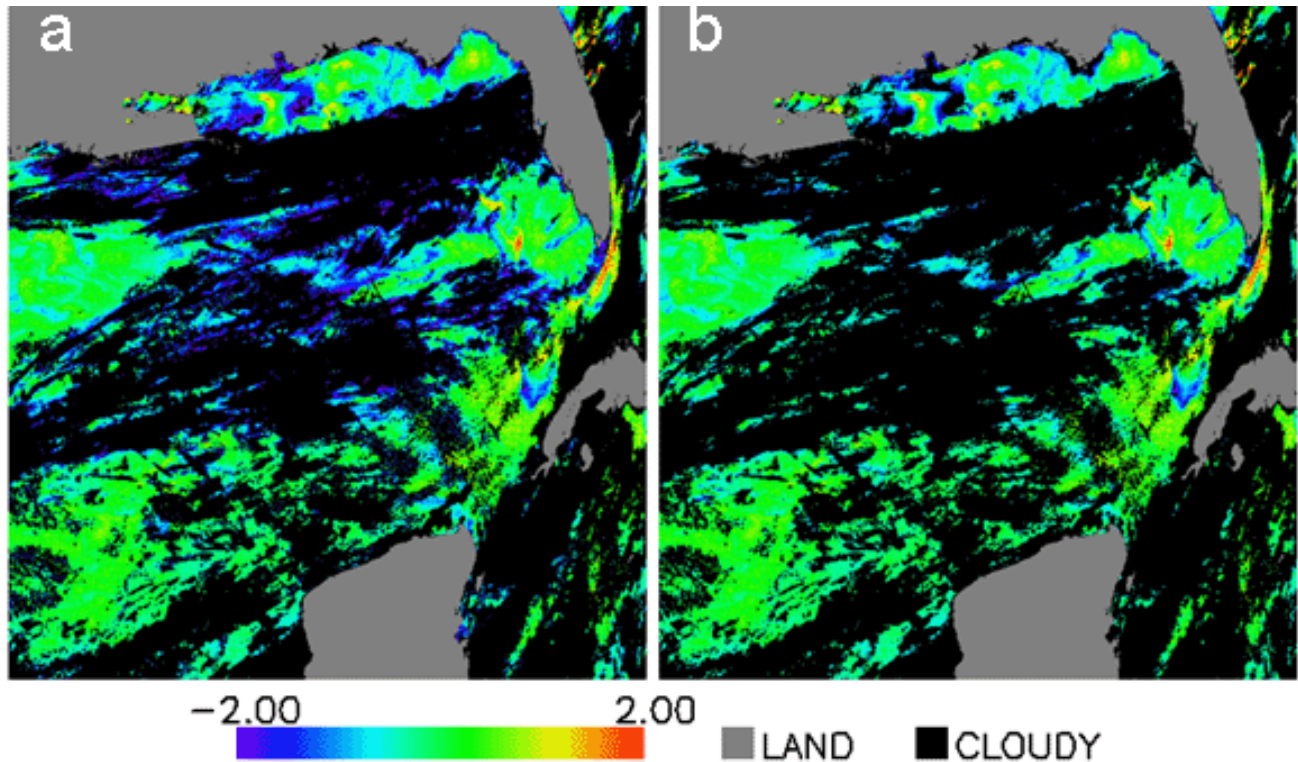
Figure 2-7
The images of SST increment, T_S-T_0, which demonstrate the results of sequential application of Static SST filter and Adaptive SST filter to the SST field produced from daytime MetOp-A observations over the Mexican Gulf on 3 February 2013. a) The cloud mask produced by the Static SST filter only; b) The cloud mask produced by sequential application of Static and Adaptive SST filters.
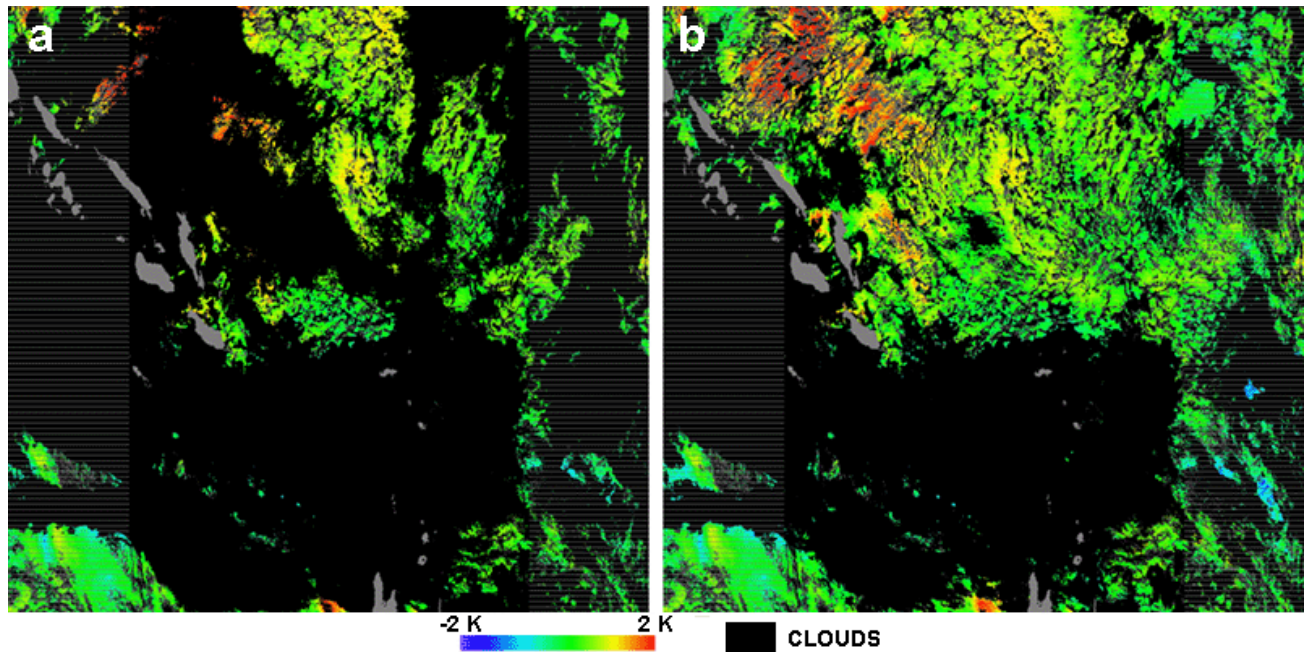
Figure 2-8
The images of ΔT$_S$, produced from daytime VIIRS observations over Pacific Ocean on 15 September 2012 with (a) ACSPO v.2.02, using for SST the formulation (3.18) of the BTF and (b) with ACSPO v. 2.2, using the formulation (3.20).
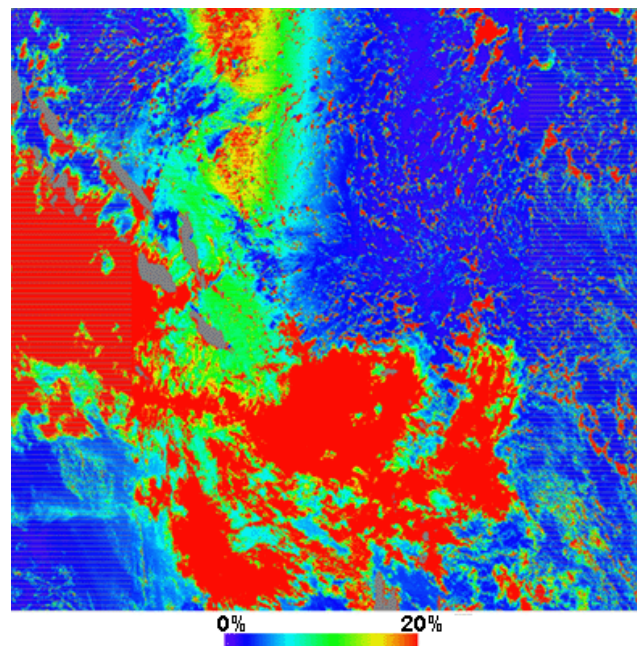
Figure 2-9
The image of reflectance in band M7 for the scene shown above.

2.3.2.3.3.4 Reflectance Gross Contrast (RGC) filter

The daytime RGC filter rejects pixels by value of observed reflectance in the VIIRS band M7(0.865 μm). The pixel is classified "Clear" if the following condition is met:

$$R_{0.87} < \zeta(\beta) \tag{2.22}$$

Here, $R_{0.87}$ is reflectance in M7 band and $\zeta(\beta)$ is a function of glint angle β. The glint angle is calculated within ACSPO as follows:

$$\beta = acos[cos(solzen)*cos(satzen)+sin(solzen)*sin(satzen)*cos(relaz)] \tag{2.23}$$

In (2.20), *solzen* is solar zenith angle, *satzen* is satellite zenith angle and *relaz* is relative azimuth. The function $\zeta(\beta)$ empirically designed to approximate the increase of clear-sky reflectance in the glint zone, this way avoiding false cloud detections:

$$\zeta(\beta)=b+c*exp[-(\beta/a)^2] \tag{2.24}$$

Here, a=18.0, b=6.0 and c=40.

Figure 2-10(a,b) demonstrates the images of SST increment, T_S-T_0, and reflectance in band M7, $R_{0.87}$. The increase of $R_{0.87}$ caused by sun glint is noticeable in Figure 2-10(b). Figure 2-10(c) shows the RGCF threshold, calculated according to (2.24). The threshold increases in the sun glint area in order to avoid false cloud detection. Figure 2-10(d,e) show the images of T_S-T_0 and $R_{0.87}$ with the cloud mask, which does not trigger on the sun glint.

2.3.2.3.3.5 Reflectance Ratio Contrast (RRC)Filter

The daytime RRC filter rejects pixels by ratio of observed reflectance in the VIIRS bands M7(0.865 μm) and M5 (0.672 μm). The pixel is classified "Clear" if the following condition is met:

$$R_{0.87} / R_{0.67} < \eta(\beta) \tag{2.25}$$

Here, $R_{0.87}$ and $R_{0.67}$ are reflectances in VIIRS bands M7 and M5 respectively and $\eta(\beta)$ is a threshold depending on glint angle β:

$$\partial(\beta)=a+b*exp[-(\beta/c)^2] \tag{2.26}$$

Here, a=0.85, b=.4 and c=35.0.

For the same scene as shown in Figure 2-10, Figure 2-11a shows the reflectance ratio, $R_{0.87}/R_{0.67}$, which increases both in cloudy pixels and in the sun glint area (cf. Figure 2-10b). Figure 2-11b shows the RCCF threshold calculated according to (2.26). The threshold

increases in the glint area to avoid triggering on sun glint. The final cloud mask (Figure 2-10(d,e) is not sensitive to the sun glint.
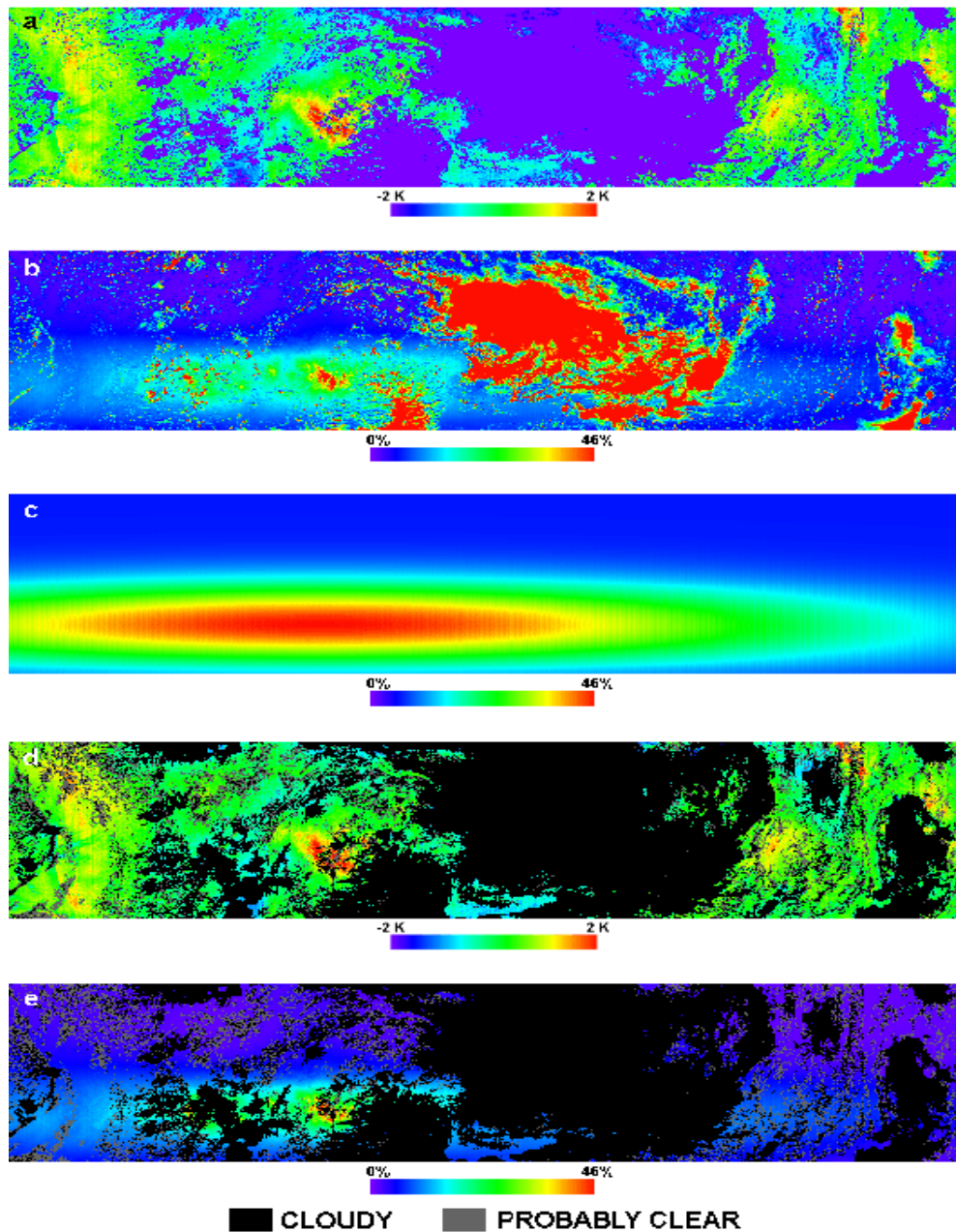
Figure 2-10
a) The image of SST increment, T_S-T_0 retrieved from daytime VIIRS observations on 24 August 2012 over Atlantic Ocean (no cloud mask); b) The image of reflectance in band M7 (no cloud mask); c) the RGCF threshold; d) The image of T_S-T_0 with imposed cloud mask; e) The image of reflectance in band M7 with imposed cloud mask. All images show the central part of the VIIRS swath, which does not include the Bow-Tie effect.
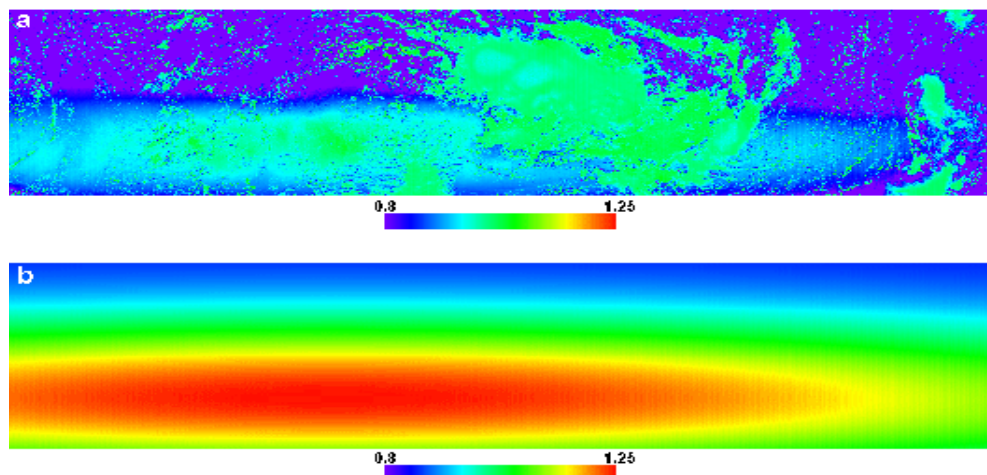
Figure 2-11
a) The image of reflectance ratio, $R_{0.87} / R_{0.67}$, for the same scene as above
b) the RCGCF threshold. Both images show the central part of the VIIRS swath, which
does not include the Bow-Tie effect.

2.3.2.3.3.6 Uniformity Filter

The five cloud filters describe above are aimed at detection of relatively intensive cloud manifestations within the fields of ΔT_S, ΔT_B and reflectance observed in VIIRS channels M7 and M5. The ACSM Uniformity filter is aimed at detection of less intensive cloud manifestations, caused by subpixel clouds, by higher spatial variability in BT and retrieved SST. The spatial uniformity (or texture) tests are used in many cloud masking algorithms. Usually, the predictors in those tests are spatial SD of variations in BT in the immediate neighborhood of a tested pixel. The potential risk of using this predictor is possible false detection of clouds in clear-sky ocean areas with high thermal gradients.

The implementation of the Uniformity filter in ACSM has the following specific features. First, it analyzes the field of retrieved SST T_S rather than observed BTs, i.e., residual cloud contaminations are detected directly within the SST product. Second, the predictor for the Uniformity test is SD of the difference $T_S - median(T_S)$ rather than SD of T_S. $Median(T_S)$ is the retrieved T_S field, passed through the 2D median filter with 3×3 window size. The median filter is known to preserve regular contrasts but suppress random noise (e.g., Gonzalez and Woods, 2003). As a result, the difference $T_S - median(T_S)$ is more sensitive to random variations in T_S, typical for the effects of sub-pixel cloud, than to more regular surface contrasts caused by ocean thermal fronts. This reduces the risk of misclassification of ocean fronts as clouds. In general, the threshold for the uniformity test is selected to be somewhat above the RMS level of random noise in SST. In the case of VIIRS, the threshold is set to make the filter insensitive to the striping noise too. Considering these factors, the threshold of the Uniformity test is set to 0.25 K for VIIRS.

Figure 2-12 demonstrates the difference in performances of the Uniformity filters using the conventional predictor – spatial SD of T_S - and the ACSPO predictor - SD of T_S – median(T_S). In Figure 2-12a, SD of T_S shows elevated values in the zones of high T_S gradients. Consequently, the Uniformity filter, using this predictor, hides large SST gradients (Figure 2-12b). In contrast, as shown in Figure 2-12c, the ACSPO predictor is almost insensitive to high T_S gradients, and, as shown in Figure 2-12d, the Uniformity filter using this predictor, preserves large SST gradients.

Figure 2-13 demonstrates the images of T_S-T_S^0 near the California coast produced from nighttime VIIRS observations on 24 August 2013. Figure 2-13a shows the field of T_S-T_S^0 with the cloud mask having the Uniformity filter turned off. Figure 2-13b shows the same field with the full cloud mask imposed, including the Uniformity filter. Comparison of the two figures shows that the Uniformity filter rejects significant amount of pixels in zones with higher and random variability in T_S but preserves large T_S gradients.
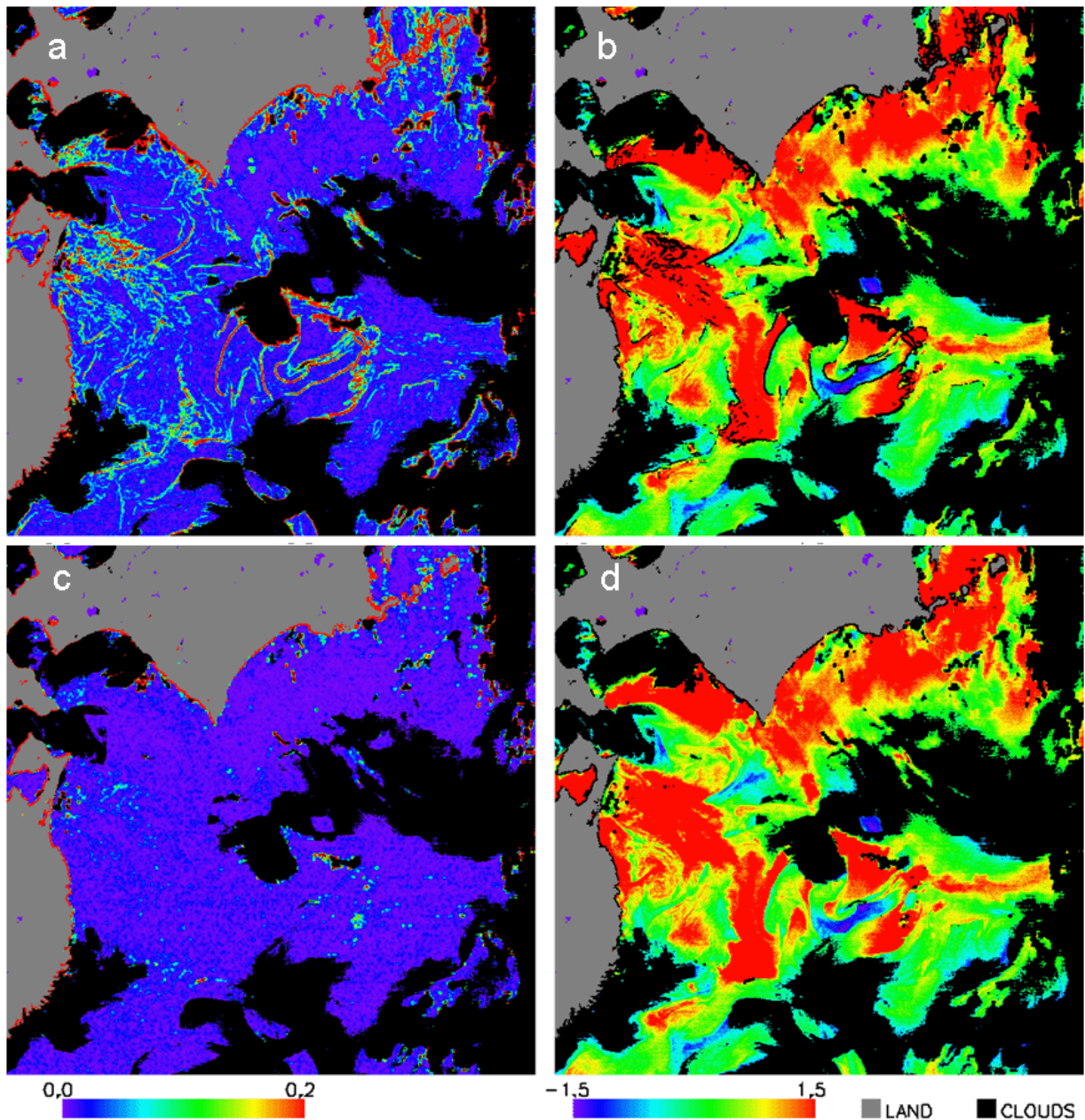
Figure 2-12
The images produced from nighttime Aqua-MODIS observations of the Pacific Ocean near Japan. a) SD of retrieved SST T_S. b) SST increment, ΔT_S. The predictor for the Uniformity filter is SD of T_S. c) SD of T_S-median(T_S). d) ΔT_S. The predictor for the Uniformity filter is SD of T_S-median(T_S).
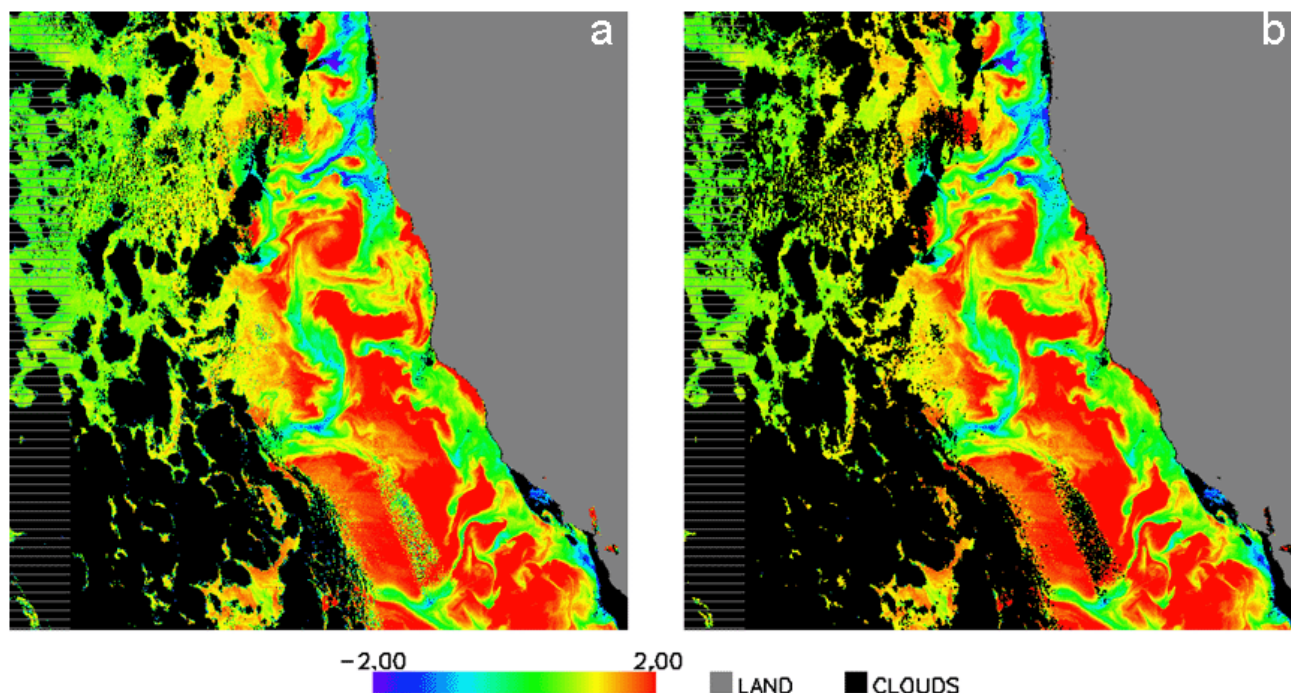
Figure 2-13

The images of ΔT_S near the California coast produced from nighttime VIIRS observations on 24 August 2013. a) Cloud mask without the Uniformity filter was used, b) Full cloud mask including the Uniformity filter was used.

2.3.2.3.3.7 SST/Reflectance Cross-Correlation (CC) filter.

The CC filter applies to the remaining "Clear" pixels downstream the Uniformity filter to detect subpixel cloud effects below the noise level by correlations of small negative deviations of SST from spatial average, with variations in reflectance in the VIIRS band M7 (0.865 µm). Because of using the reflectance band, this filter can be used only in the daytime. The predictor for the CC filter is constructed as follows.

1. If the pixel is not "Clear" the next pixel
2. If $R_{0.87} < 0.5\%$ then go to the next pixel
3. Calculate spatial mean $<T_S>$ of T_S within the 3×3 sliding window surrounding the tested pixel.
4. If $T_S \geq <T_S>$ then go to the next pixel
5. Calculate spatial variance of T_S:

$$D = <(T_S - <T_S>)^2> \tag{2.24}$$

6. Calculate spatial correlation of T_S and $R_{0.87}$ within the sliding window:

$$r = <(T_S - <T_S>)(R_{0.87} - <R_{0.87}>)>/[D*<(R_{0.87} - <R_{0.87}>)^2>]^{1/2} \tag{2.25}$$

7. If r>0 then go to the next "Clear" pixel
8. Calculate the part d of T_S spatial variance D, explained by variations in $R_{0.87}$:

$$d = r^2 D \tag{2.26}$$

9. If $d > \delta$ then reclassify the tested pixel as "Probably Clear" and go to the next pixel.

The above algorithm contains a number of conditions which should be met for the test to be applied to a given pixel. These conditions are:
- The pixel is initially "Clear" (Condition 1)
- The M7 reflectance in this pixel $R_{0.87} \geq 0.5\%$ (Condition 2)
- T_S in the tested pixel is < than spatial average $<T_S>$ (Condition 4)
- The covariation between T_S and $R_{0.87}$ is negative within the sliding window (Condition 7)

Figure 2-14 demonstrates the performance of the CC filter. Figure 2-14a and Figure 2-14b are the images of $R_{0.87}$ and T_S-T_S^0 with the cloud mask including all filters except CC. The pixels containing residual subpixel cloud are recognized on these images by $R_{0.87}$ being brighter than the background and T_S being colder than in neighboring pixels. However, the detection of subpixel clouds by only one of these two effects would cause multiple cloud misdetections due to striping noise clearly seen in both images, and random noise in Figure 2-14b. Figure 2-13c and Figure 2-13d, which show the same images of $R_{0.87}$ and T_S-T_S^0 with the full cloud mask, including the CC filter, demonstrate that accounting for correlation between the two variables allows effective detection of small cloud effects on the background of thermal and striping noise.
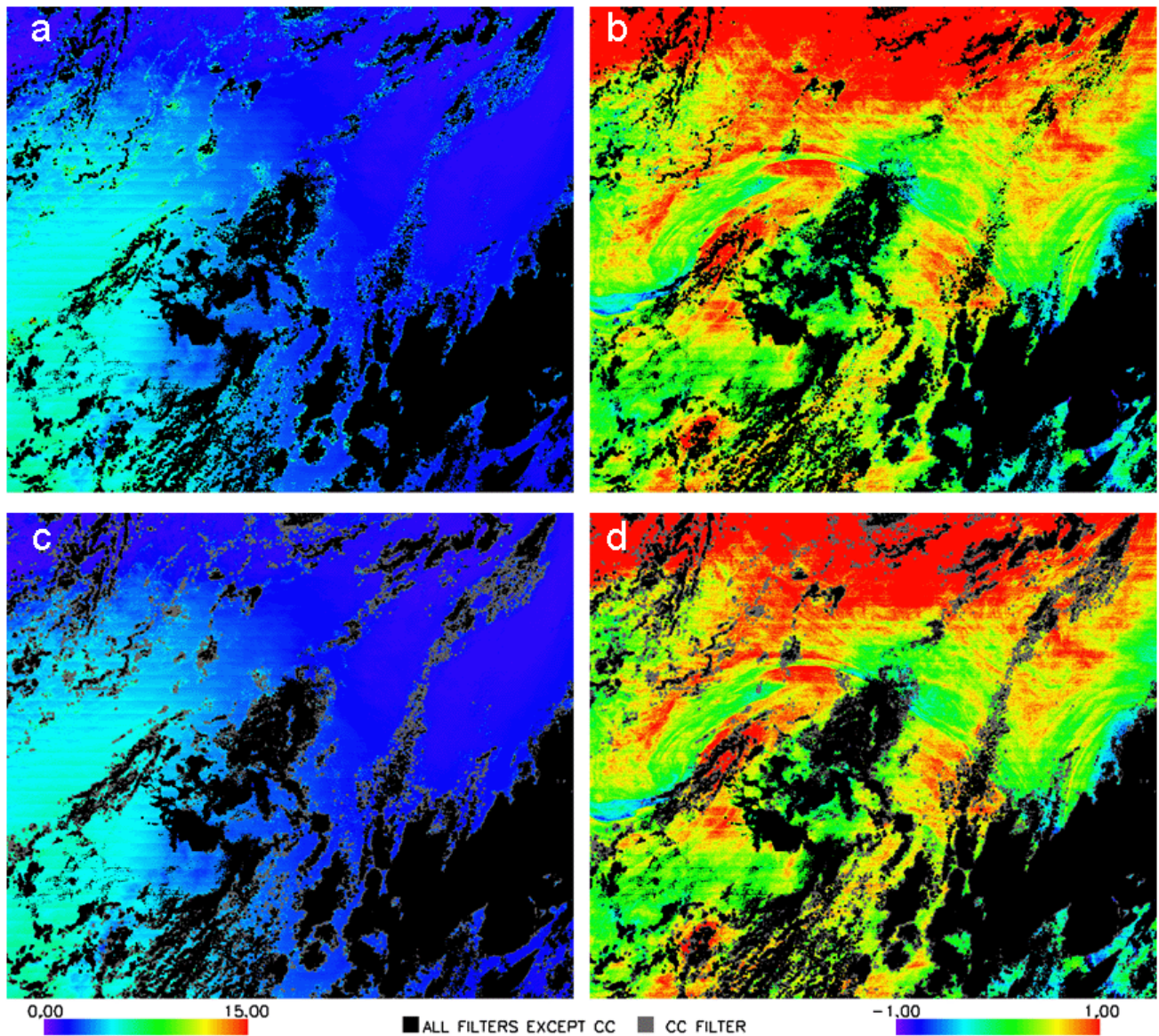
Figure 2-14
a) Reflectance in VIIRS M7 band and b) T_S-T_S^0 form daytime VIIRS observations over Pacific Ocean on 24 August 2012. The imposed cloud mask does not include the CC filter. c) Reflectance in VIIRS M7 band and d) T_S-T_S^0 with the full cloud mask imposed, including the CC filter.

2.4   Algorithm Output

ACSPO generates a number of output products. The two main products are the SST and ACSPO Clear-Sky Mask (ACSM). In addition, the following products are also generated:
- brightness temperatures (BTs) for each thermal channel – For AVHRR and MODIS these are calculated from the input L1b radiances. For VIIRS these are passed through from the input SDR data.
- geo-location angles – For the most part, these are passed through from the input geo-location data, but some may be calculated
- albedos for each reflectance channel – Calculated albedo data from the input reflectance data
- simulated BTs for each thermal channel – These are calculated by CRTM and primarily used for offline monitoring of the BT data
- reference SST – The input gridded L4 SST data interpolated to the swath. Used as a first-guess in the regression SST calculation, in offline monitoring of calculated SSTs, and as input to CRTM.
- forecast model data – The input gridded forecast (e.g., GFS) data interpolated to the swath
- surface properties data –Land/water distances and bathymetry data interpolated to the swath

All of the above products are generated for every valid ocean pixel.

2.5   Performance Estimates

2.5.1   Test Data Description

The ACSPO VIIRS SST L2 product has been generated at STAR since January 2012. Since that time, the performance of VIIRS SST has been routinely monitored in SST Quality Monitor (SQUAM, available at http://www.star.nesdis.noaa.gov/sod/sst/squam/index.html) and in Monitoring of IR Clear-Sky Radiances over Oceans for SST (MICROS, available at http://www.star.nesdis.noaa.gov/sod/sst/micros/). The performance of the SST products is evaluated by comparisons with other L2 products from AVHRRs, MODIS and VIIRS instruments, L4 SST fields (such as Reynolds, OSTIA etc.) and with quality *in situ* SST data, selected at In situ SST Quality Monitor (iQuam, available at http://www.star.nesdis.noaa.gov/sod/sst/iquam/).

2.5.2   Sensor Effects

The VIIRS SST is affected by the thermal noise and the striping noise. On-orbit estimates of the thermal noise in the reflectance bands (SNR) and in thermal bands (NEdT) are shown in Table 1-2. The striping noise is caused by using16 separate detectors, having slightly different calibrations, to simultaneously track 16 sequential rows.

The examples of thermal and striping noise in the M5 band and in SST can be seen in Figure 2-14. The algorithm for de-striping VIIRS data is currently being developed at STAR (Bouali and Ladjal, 2011; Bouali and Ignatov, 2013a, 2013b) and is planned to be incorporated in ACSPO in the future.

A certain impact on the VIIRS SST product can have the deletion of pixels in the 2 pixel aggregation zones at edges of the 1st, the 2nd, the 15th and the 16th scans in every series of 16 scans, simultaneously produced by 16 detectors (Baker, 2011). This results in a loss of 1008 pixels at the edges of the 1st and the 16th scans and 640 pixels at the edges of the 2nd and the 15th scan. Due to this effect, the performance of ACSM filters using spatial windows (such as Static and Adaptive SST, Uniformity and CC filters) can degrade in the peripheral parts of the swath. However, by the time of this writing no negative effects of this kind have been noticed yet.

2.5.3   Retrieval Errors

Figure 2-15 demonstrates day- and nighttime histograms of VIIRS ACSPO SST – *in situ* SST accumulated during May 2013. Both histograms have a quasi-Gaussian shape. The

statistics are shown on the left-hand sides of each plot. The retrieval accuracy (Mean) and the precision (Stdv) are well within the threshold requirements listed in Table 1-1 (0.2 K and 0.6 K respectively) and the accuracy is close to or better than the objective requirement (0.5 K) listed in this table. Figure 2-16 and Figure 2-17 plot the time series of monthly averaged bias and standard deviation of ACSPO SST minus *in situ* SST for several satellite sensors and processing systems. The retrieval statistics of ACSPO VIIRS SST are stable in time and consistent with or better than for other satellite SST products. The daytime and nighttime composite maps of ACSPO VIIRS SST – OSTIA produced from VIIRS data for 20 May 2013 and shown in Figure 2-18 and Figure 2-19 demonstrate a good consistency of ACSPO VIIRS SST with L4 analyses SST field. The daytime and nighttime histograms and statistics of ACSPO VIIRS SST – OSTIA for the same day are shown in Figure 2-20 and Figure 2-21.
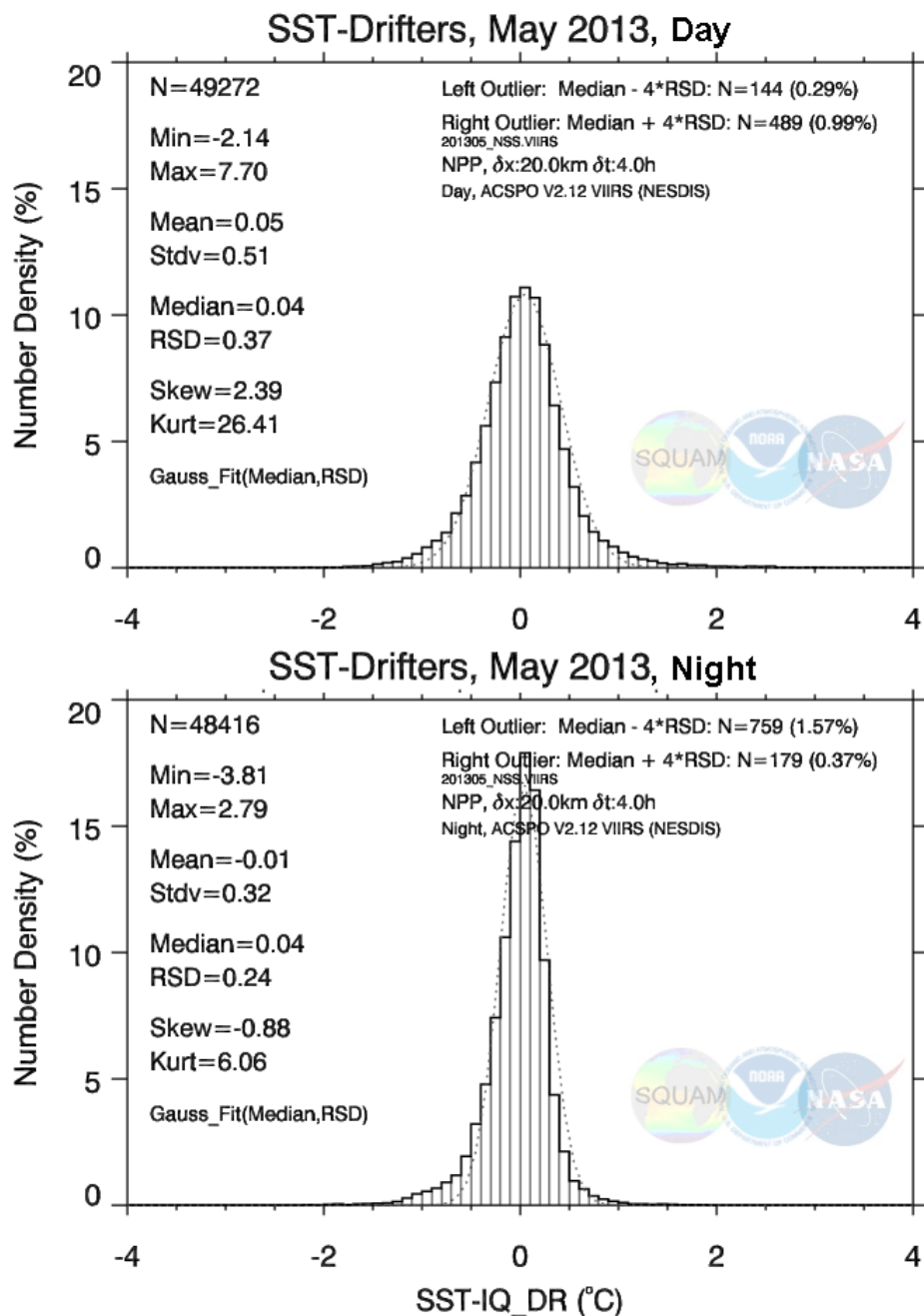
Figure 2-15
Daytime and nighttime histograms of ACSPO VIIRS SST minus in situ SST accumulated
during May 2013 (from http://www.star.nesdis.noaa.gov/sod/sst/squam/HR/index.html)
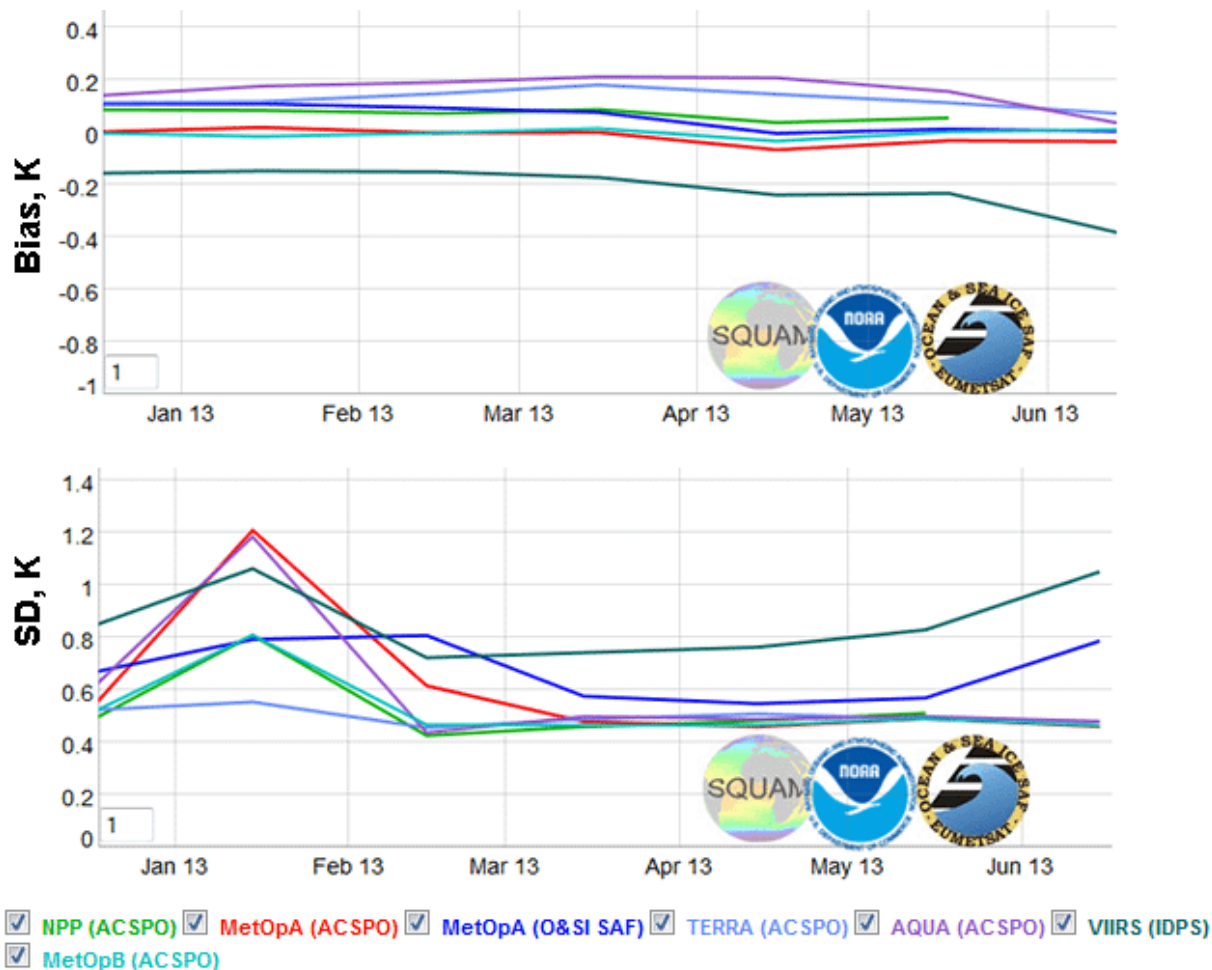
Figure 2-16
Time series of daytime monthly bias and SD of retrieved SST minus in situ SST for several satellite sensors and processing systems (from http://www.star.nesdis.noaa.gov/sod/sst/squam/HR/index.html)

- *NPP(ACSPO) is VIIRS SST produced with ACSPO;*
- *MetOpA(ACSPO) and MetOpB(ACSPO) are the ACSPO products from the MetOp-A and MetOp-B AVHRRs;*
- *MetOpA(O&SI SAF) is SST produced from the MetOp-A AVHRR at OSI-SAF; TERRA(ACSPO) and AQUA(ACSPO) are the ACSPO products from Aqua and Terra MODIS;*
- *VIIRS(IDPS) is SST produced from VIIRS with the Interface Data Processing System;*
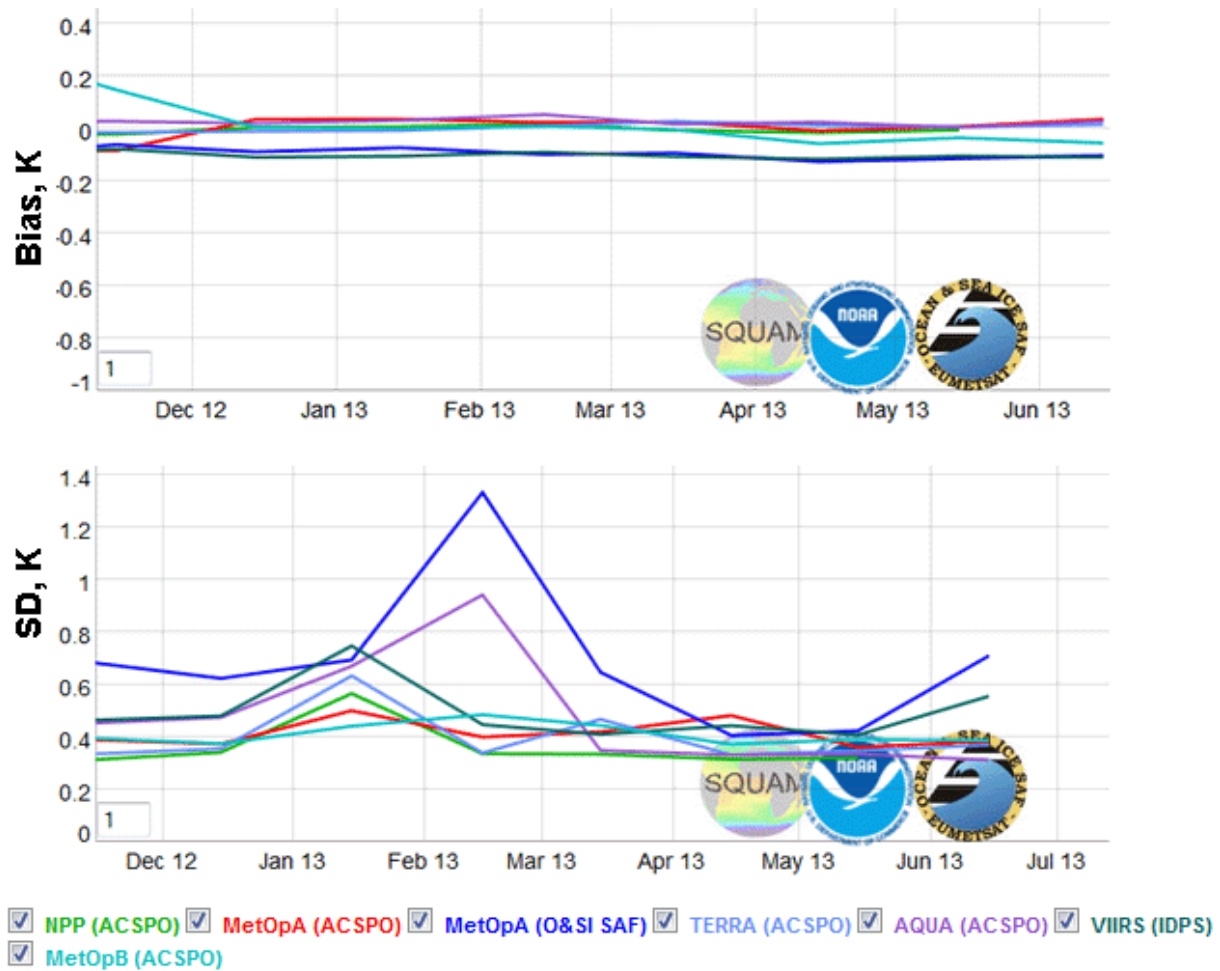
Figure 2-17
*Time series of nighttime monthly bias and SD of retrieved SST minus in situ SST for the
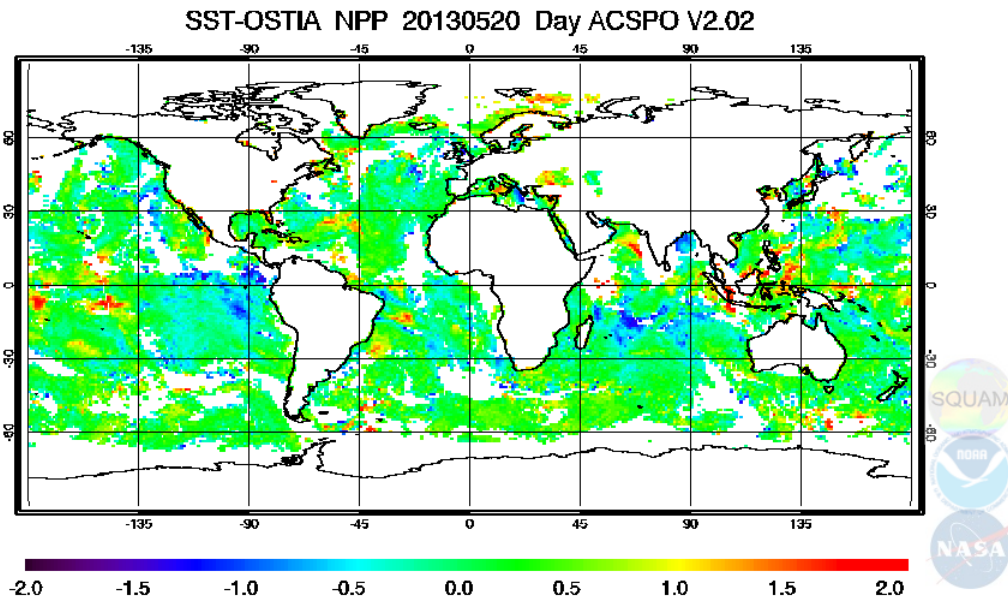same satellite sensors and processing systems as listed above (from
http://www.star.nesdis.noaa.gov/sod/sst/squam/HR/index.html)*

Figure 2-18
Global composite map of ACSPO VIIRS SST – OSTIA for 20 May 2013 (from http://www.star.nesdis.noaa.gov/sod/sst/squam/HR/index.html)
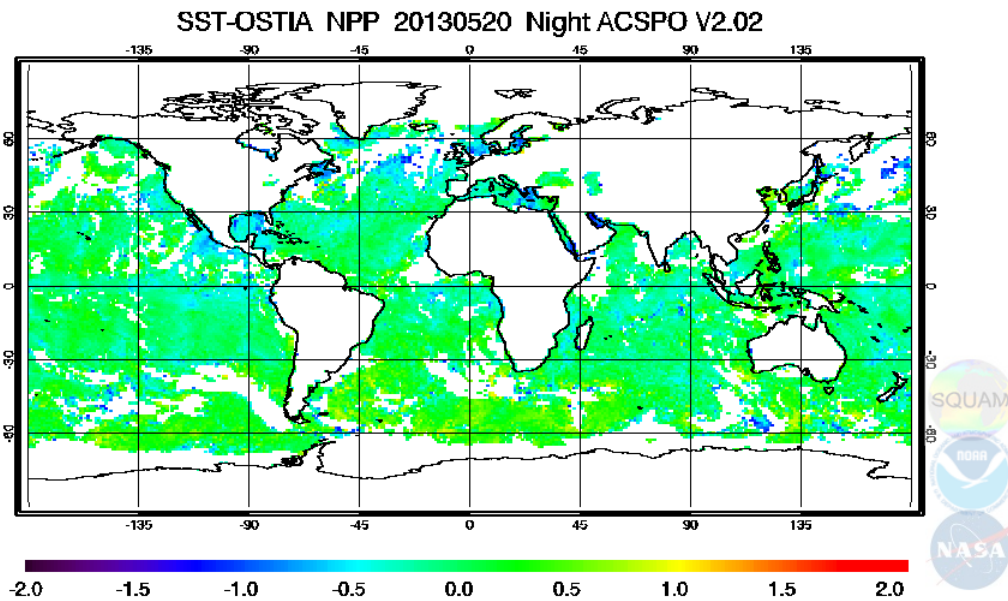
Figure 2-19
Global composite map of ACSPO VIIRS SST – OSTIA for 20 May 2013 (from http://www.star.nesdis.noaa.gov/sod/sst/squam/HR/index.html)
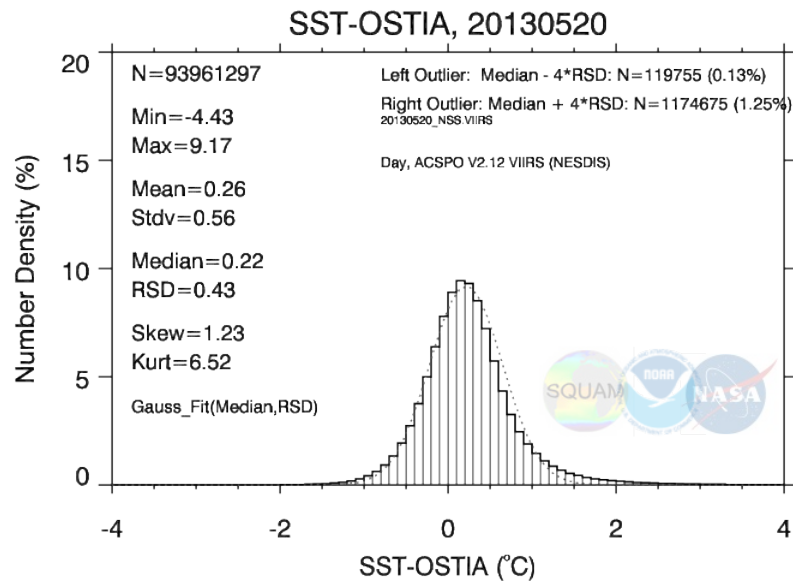
Figure 2-20
Daytime histogram of ACSPO VIIRS SST – OSTIA for 20 May 2013 (from
http://www.star.nesdis.noaa.gov/sod/sst/squam/HR/index.html)
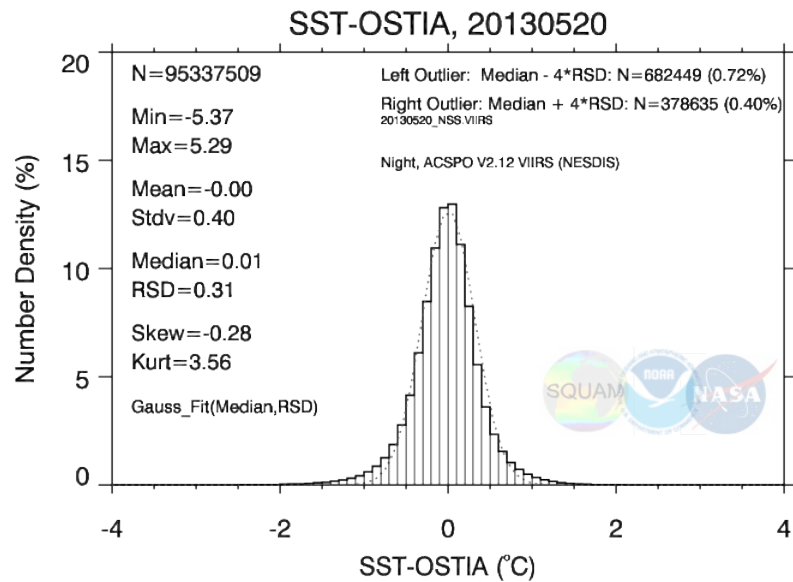
Figure 2-21
Nightime histogram of ACSPO VIIRS SST – OSTIA for 20 May 2013 (from
http://www.star.nesdis.noaa.gov/sod/sst/squam/HR/index.html)

2.6   Practical Considerations

2.6.1   Numerical Computation Considerations

ACSPO is written in Fortran 2003 and runs on both the Linux and AIX platforms. Most of its calculations are performed using single-precision computations. Its testing has not revealed any numerical instability in the underlying algorithms over the range of conditions evaluated. Its computationally intensive operations are primarily related with CRTM radiative transfer simulations, those ACSM filters that use spatial windows, and bilinear interpolation (primarily, because of the many times it is called).

The processing time for a file depends on many factors including the platform/machine, how well the parallel processing (i.e., OpenMP) environment is tuned to that machine, the input data itself (e.g., instrument being processed, complexity of the scene data), and even the number of files processed during a single ACSPO run (generally, the more the better). For example, multiple 10-minute VIIRS granules processed together during a single run of ACSPO on the Linux platform averages about 2 minutes per granule. Whereas, a single 10-minute VIIRS granule processed on the AIX platform takes closer to 7 minutes.

Some of the techniques employed to help reduce the ACSPO processing time include
- built-in array processing, where possible (instead of processing each array element individually).
- a user-specifiable configuration parameter to define a larger segment size. Larger amounts of data processed at one time results in faster processing times. However, the larger the segment size, the more memory that is required.
- OpenMP directives to allow for multi-threaded processing. By default these directives are turned on via a specific compiler flag. When turned on, a set of environment variables can be defined during run-time to control the multi-threaded execution, including the number of CPUs used, resulting in significant reduction in overall processing time.

Outside of the ACSPO algorithm, the NDE operating environment is likely to implement load balancing to optimize throughput in order to keep up with the real-time data flow.

Because of the use of the input/output histogram files, a dependency exists between granules. Thus, granules must be, as much as possible, processed in chronological order, and as such, can't be farmed out to multiple processors for simultaneous processing.

2.6.2   Programming and Procedural Considerations

The ACSPO code is already fully mature and has been tested with multiple compilers (Intel, PGI, XLF) on multiple platforms (Linux and AIX). All models and algorithms have been

used at STAR and OSPO for processing data from a number of satellite sensors for several years. (ACSPO first went operational in May 2008.) The code consists of several separate modules, all with well-defined interfaces, where each module is driven by its own configuration file. Except for the sensor module, which must be specific to the input satellite data it handles, the modules are flexible and can be applied to different sensors without modifications. This should simplify any updates or additions that may be made to the ACSPO code in the future. In addition, all code is configuration managed within a CVS repository. Thus, a history of the code is maintained here so that any prior version of the code can be easily retrieved.

2.6.3 Quality Assessment and Diagnostics

The ACSPO VIIRS SST L2 product has been generated at STAR since January 2012. Since that time, the performance of VIIRS SST has been routinely monitored in SST Quality Monitor (SQUAM, available at http://www.star.nesdis.noaa.gov/sod/sst/squam/index.html) and in Monitoring of IR Clear-Sky Radiances over Oceans for SST (MICROS, available at http://www.star.nesdis.noaa.gov/sod/sst/micros/). The performance of the SST products is evaluated by comparisons with other L2 products from AVHRRs, MODIS and VIIRS instruments, L4 SST fields (such as Reynolds, OSTIA etc.) and with quality *in situ* SST data, selected at In situ SST Quality Monitor (iQuam, available at http://www.star.nesdis.noaa.gov/sod/sst/iquam/).

2.6.4 Exception Handling

Input pixels with poor quality and land pixels are skipped. ACSPO expects the three BT channels (3b, 4, 5 for AVHRR; 20, 31, 32 for MODIS; M12, M15, M16 for VIIRS), geo-location data, and all necessary ancillary data to be present. If any of these are not available, appropriate error messages are generated, but no processing is performed.

Also, ASCPO has a couple of built-in graceful degradation features that allow it to run successfully even with sub-optimal input data. First, given a directory of GFS or reference SST ancillary files and using the time of the satellite data being processed, ACSPO selects the temporally closest file(s) from this directory. The user does not need to specify a specific file or be concerned that the latest file is not available. Second, ACSPO runs normally if any of the input histogram files are not available. In either case (not the latest ancillary file or missing histogram file), degradation in quality will be seen in the ACSPO products.

2.7   Validation

Validation of the ACSPO VIIRS SST product is performed by comparisons with *in situ* SST measurements, L4 analysis SST fields and with SST produced from other satellite sensors. This is done routinely and online in SST Quality Monitor (SQUAM, available at http://www.star.nesdis.noaa.gov/sod/sst/squam/index.html) and in Monitoring of IR Clear-Sky Radiances over Oceans for SST (MICROS, available at http://www.star.nesdis.noaa.gov/sod/sst/micros/). The examples of VIIRS SST validation are given in Section 2.5.3.

3   ASSUMPTIONS AND LIMITATIONS

3.1   Performance Assumptions

The ACSPO SST algorithm is intended to retrieve SST in clear-sky conditions only. The special ACSPO module, the ACSPO Clear-Sky Mask (ACSM), identifies cloudy pixels and marks them with special quality flags. In clear-sky situation, the SST accuracy and precision retrieval can degrade due to abnormal water vapor distributions in the atmosphere and abnormally high concentrations of the atmospheric aerosol (e.g., Saharan dust). The ACSM partially handles those situations, however some errors in SST are possible due to imperfect filtering of clouds and abnormal attenuation in the clear-sky atmosphere.

3.2   Potential Improvements

The ACSPO functionality is continuously improved as new ACSPO versions are created. The main directions of potential improvements are:
1. Implementation of more accurate SST algorithms. Recently, more efficient SST algorithms than one currently used in ACSPO have been identified based on comprehensive evaluation of existing regression SST algorithms (Petrenko et al., 2013a). These algorithms will be implemented in one of the future ACSPO version. In addition, the Incremental Regression, or Hybrid SST algorithm, earlier developed for the MSG-2 SEVIRI instrument (Petrenko et al., 2011) is currently being tested within the experimental ACSPO version for NOAA and MetOp AVHRRs and can replace the regression algorithm in the future.
2. The improvement of the ACSPO Clear-Sky Mask (ACSM). The performance of the current version of the ACSM is well on par with other existing operational products. However, the search of potential improvements to the ACSM is currently underway. In particular, the potential of the cloud filters based on the pattern recognition techniques is currently being explored (Gladkova et al., 2013).

3. The algorithm for de-striping VIIRS data is currently being developed at STAR
    (Bouali and Ladjal, 2011; Bouali and Ignatov, 2013a, 2013b) and will be a part of the
    ACSPO in the future.

4   REFERENCES

Baker, N., 2011: Joint Polar Satellite System (JPPS) VIIRS Geolocation Algorithm
    Theoretical Basis Document (ATBD),
    http://npp.gsfc.nasa.gov/science/sciencedocuments/ATBD_122011/474-
    00053_Geolocation_ATBD_Rev-_20110422.pdf

Bouali, M. and S. Ladjal, 2011: Toward optimal destriping of MODIS data using a
    unidirectional variational model. IEEE Trans. Geosci. Remote Sens., 49 (8), 2924--
    2935.

Bouali, M. and A. Ignatov, 2013a: Estimation of detector biases in MODIS thermal emissive
    bands. IEEE Trans. Geosci. Remote Sens., 51 (7), 4339—4349

Bouali, M. and A. Ignatov, 2013b: Adaptive Reduction of Striping for Improved Sea Surface
    Temperature Imagery from Suomi National Polar-orbiting Partnership (S-NPP) Visible
    Infrared Imaging Radiometer Suite (VIIRS), JTech (in review)

Castro S.L., G.A. Wick & W.J. Emery, 2003: Further refinements to models for the bulk-skin
    SST difference. *JGR*, 108, 3377, doi:10.1029/2002JC001641

Castro S.L., G.A. Wick, D.L. Jackson, & W.J. Emery, 2008: Error characterization of
    infrared and microwave satellite SST products for merging and analysis. *JGR*, 113,
    C03010, doi:10.1029/2006JC003829

Chen, Y., F. Weng, Y. Han, and Q. Liu (2012a), Planck weighted transmittance and
    correction of solar reflection for broadband infrared satellite channels. *J. Atmos.
    Ocean. Technol.*, 29, 382–396. doi:10.1175/JTECH-D-11-00102.1.

Chen, Y., Y. Han, and F. Weng (2012b), 384 Comparison of two transmittance algorithms
    in the Community Radiative Transfer Model: Application to AVHRR. *J. Geophys. Res.*,
    117, D06206,386 doi:10.1029/2011JD016656.

Chin, M., R.B. Rood, S.-J. Lin, J.F. Muller & A.M. Thomspon, 2000: Atmospheric sulfur
    cycle in the global model GOCART: Model description and global properties, *JGR*,
    105, 24,671-24,687

Dash, P. and A. Ignatov, 2008: Validation of Clear-Sky Radiances over Oceans Simulated with MODTRAN4.2 and Global NCEP GDAS Fields against nighttime NOAA15-18 and MetOp-A AVHRR Data. *RSE*, 112, 3012-3029

Donlon, C.J., S.J. Keogh, D.J. Baldwin, et al, 1998: Solid-state radiometer measurements of skin SST. *JTech*, 15, 775-787

Donlon, C. J., P. J. Minnett, C. Gentemann, T. J. Nightingale, I. J. Barton, B. Ward, and J. Murray, 2002: Toward improved validation of satellite sea surface skin temperature measurements for climate research. *Journal of Climate*, **15,** 353-369

Donlon, C., N. **Rayner, I. Robinson, et al. (2007),** The Global Ocean Data Assimilation Experiment High-resolution Sea Surface Temperature Pilot Project, *Bull. Am. Meteorol. Soc.*, **88**, 1197–1213

Donlon, C., M. Martin, J. Stark, J. Roberts-Jones, E. Fiedler, and W. Wimmer, (2012), The operational sea surface temperature and Sea Ice Analysis (OSTIA) system. *Remote Sens. Environ.*, **116**, 140–158

Downing, H.D., & D. Williams, 1975: Optical constants of water in the infrared. *JGR*, 80, 1656–1661

Fairall, C.W. et al, 1996: Cool-skin and warm-layer effects on SST. *JGR*, 101, 1295-1308

Franz, B. (2009), Implementation of SST Processing within the OBPG. http://oceancolor.gsfc.nasa.gov/DOCS/modis_sst/

Friedman, D., 1969: Infrared characteristics of ocean water (1.5-15 µm). *Appl. Opt.*, 8, 2073–2078

Gentemann, C. L., C. J. Donlon, A. Stuart-Menteth, and F. J. Wentz, 2003: Diurnal signals in satellite sea surface temperature measurements. *Geophysical Research Letters*, **30,** 1140-1143

Gentemann, C. L. and P. J. Minnett, 2008: Radiometric measurements of ocean surface thermal variability. *Journal of Geophysical Research*, **113,** C08017.doi:10.1029/2007JC004540

Gladkova, I., F. Shahriar, Y. Kihai, B. Petrenko, A. Ignatov, M. Bouali and M. Grossberg, 2013: Pattern recognition enhancements to NOAA ACSPO Clear-Sky Mask. *Presentation at the GHRSST XIV Science Team Meeting, Woods Hole, MA, USA, 17-*

21 June 2013, https://www.ghrsst.org/ghrsst-science/Meetings-and-workshops/ghrsst-xiv-science-team-meeting/

Gonzalez, R.C., and R. E. Woods, 2003: Digital image processing. Pearson Education (Singapore) Pte. Ltd., 793 pp

Hale, G.M. & M.R. Querry, 1973: Optical constants of water in the 200-nm to 200-μm wavelength region. *Appl. Opt.*, 12, 555–563

Han, Y., P. van Delst, Q. Liu, F. Weng, B. Yan, R. Treadon, and J. Derber (2006), Community Radiative Transfer Model (CRTM)-Version 1, NOAA Technical Report, NESDIS 122, 40 pp.

Hanafin, J.A. & P.J. Minnett, 2005: Measurements of the infrared emissivity of a wind-roughened sea surface. *Appl. Opt.*, 44 (3), 398-411

Highwood, E.J., J.M. Haywood, M.D. Silverstone, S.M. Newman & J.P. Taylor, 2003: Radiative properties and direct effect of Saharan dust measured by the C-130 aircraft during Saharan Dust Experiment (SHADE): 2. Terrestrial spectrum. *JGR*, 108, DOI:10.1029/2002JD002552

Hollweg, H.-D., S. Bakan & J.P. Taylor, 2006: Is the aerosol emission detectable in the thermal Infrared? *JGR*, DOI:10.1029/2005JD006432, D15202, 111, 1-13

Horrocks, L. A., B. Candy, T. J. Nightingale, R. W. Saunders, A. O'Carroll, and A. R. Harris, 2003: Parameterizations of the ocean skin effect and implications for satellite-based measurement of sea-surface temperature. *Journal of Geophysical Research*, **108,** 3096

Ignatov, A. et al., 2010: GOES-R advanced baseline imager (ABI) ATBD for SST. NOAA/NESDIS/STAR, 2010. http://goesrtest2.woc.noaa.gov/products/ATBDs/baseline/baseline-SST-v2.0.pdf

Ignatov A., J. Sapper, Y. Kihai, et al., (2012), Polar SST Products and Monitoring at NESDIS. 13th GHRSST meeting, 4-8 June 2012, Tokyo, Japan. https://www.ghrsst.org/files/download.php?m=documents&f=120611145909-1120120604ACSPOMonitoringIgnatovv04.pdf

Jackson, S., and P.D. Siebels, (2011). Operational Algorithm Description Document for VIIRS Sea Surface Temperature (SST) EDR, http://npp.gsfc.nasa.gov/science/sciencedocuments/022012/474-00061_OAD-VIIRS-SST-EDR-SW_RevA_20120127.pdf

Joint Polar Satellite System (JPSS) Program Level 1 Requirements. Supplement – final, January 30, 2013

Khattak, S., RA. Vaughan, & AP. Cracknell, 1991: Sunglint and its observation in AVHRR data. *RSE*, 37, 101-116

Kilpatrick, K.A., G.P. Podesta, and R. Evans (2001), Overview of the NOAA/NASA advanced very high resolution radiometer Pathfinder algorithm for sea surface temperature and associated matchup database, *J. Geophys. Res.*, **106**, *C5,* 9179-9297

Lavanant, L., P. Le Borgne, G. Legendre, A. Marsouin, S. Pere, and H. Roquet (2012), VIIRS SST at OSI-SAF. GHRSST XIII Science Team Meeting, Tokyo, Japan https://www.ghrsst.org/files/download.php?m=documents&f=120618134746-GHRSSTXIIIviirsosisaf3.pdf

Le Borgne, P., H. Roquet, and C.J. Merchant (2011), Estimation of sea surface temperature from the Spinning Enhanced Visible and Infrared Imager, improved using numerical weather prediction, *Remote Sens. Environ.*, **115**, 55–65

Llewellyn-Jones, D.T., P.J. Minnett, R.W. Saunders & A.M. Zavody, 1984: Satellite multi-channel infrared measurements of SST of the N.E. Atlantic Ocean using AVHRR/2. *QJRMS*, 110, 613-631

Liang, X., A. Ignatov, and Y. Kihai (2009), Implementation of the Community Radiative Transfer Model (CRTM) in Advanced Clear-Sky Processor for Oceans (ACSPO) and validation against nighttime radiances. *J. Geophys. Res.*, **114**, *D06112*, doi: 10.1029/2008JD010960.

Liang, X. and A. Ignatov (2013), AVHRR, MODIS and VIIRS radiometric stability and consistency in SST bands. *J. Geophys. Res.*, in press.

Masuda, K., 2006: Infrared sea surface emissivity including multiple reflection effect for isotropic Gaussian slope distribution model. *RSE*, 103, 488–496

McClain, E. P., W. G. Pichel, C. C. Walton, Z. Ahmad, and J. Sutton, 1983: Multi-channel improvements satellite derived global sea surface temperatures. *Adv. Space Res.*, **2,** 43-47

McMillin, L., 1975: Estimation of sea-surface temperatures from two infrared window measurements with different absorption. *J. Geophys. Research*, **80,** 5113-5117

Merchant, C.J. & A.R. Harris, 1999: Towards the elimination of bias in satellite retrievals of SSTs. 2: Comparison with *in situ* measurements. *JGR*, 104, 23,579-23,590.

Merchant, C.J., O. Embury, P. Le Borgne & B. Bellec, 2006: Saharan dust in nighttime thermal imagery: Detection and reduction of related biases in retrieved SST. *RSE*, 104 (1), 15-30.

Merchant, C. J., P. Le Borgne, P., H. Roquet, and A. Marsouin (2009), Sea surface temperature from a geostationary satellite by optimal estimation, *Remote Sens. Environ.*, **113**, 445–457

Minnett, P.J., R.O. Knuteson, F.A. Best, B.J. Osborne, J.A. Hanafin & O.B. Brown, 2001: The Marine-Atmospheric Emitted Radiance Interferometer: A high-accuracy, seagoing infrared spectroradiometer. *JTech*, 18, 994-1013

Minnett, P. J., 2003: Radiometric measurements of the sea-surface skin temperature - the competing roles of the diurnal thermocline and the cool skin. *International Journal of Remote Sensing*, **24,** 5033-5047

Minnett, P.J., O.B. Brown, R.H. Evans, E.L. Key, E.J. Kearns, K. Kilpatrick, A. Kumar, K.A. Maillet, and G. Szczodrak (2004), Sea-surface temperature measurements from the Moderate-Resolution Imaging Spectroradiometer (MODIS) on Aqua and Terra, Geoscience and Remote Sensing Symposium, Proc. IGARSS '04, 7, 4576–4579

Murray, J.M., M.R. Allen, C.J. Merchant, A.R. Harris & C.J. Donlon, 2000: Direct observations of skin-bulk SST variability. *GRL*, 27, 1171–1174

Nalli, N.R. & L.L. Stowe, 2002: Aerosol correction for remotely sensed SSTs from the NOAA AVHRR. *JGR*, 107, 3172

Nalli, N.R. & R.W. Reynolds, 2006: SST Daytime Climate Analyses Derived from Aerosol Bias-Corrected Satellite Data. *JClim*, 19, 410–428

Nardielli, B.B., S. Marullo, R. Santoleri, 2005: Diurnal variations in AVHRR SST fields: A strategy for removing warm layer effects from daily images. *RSE*, 95, 47-56

Nath, AN., MV. Rao, & KH. Rao, 1993: Observed high temperatures in the sunglint area over the North Indian Ocean. *IJRS*, 14, 849-853

Newman, S.M., J.A. Smith, M.D. Glew, S.M. Rogers & J.P. Taylor, 2005: Temperature and salinity dependence of sea surface emissivity in the thermal infrared. *QJRMS*, 131, 2539-2557

Niclòs, R., E. Valor, V. Caselles, C. Coll & J.M. Sanchez, 2005: *In situ* angular measurements of thermal infrared sea surface emissivity--Validation of models. *RSE*, 94, 83-93

OSI-SAF Low Earth Orbiter Sea Surface Temperature Product User Manual, Version 2.1. The EUMETSAT Network of Satellite Application Facilities, OSI-SAF (2009), http://www.osi-saf.org/biblio/docs/ss1_pum_leo_sst_2_1.pdf

Petrenko, B., A. Ignatov, Y. Kihai, and A. Heidinger (2010), Clear-sky mask for the Advanced Clear-Sky Processor for Oceans, *J. Atmos. Oceanic Technol.*, **27**, 1609–1623.

Petrenko, B., A. Ignatov, N. Shabanov, and Y. Kihai (2011), Development and evaluation of SST algorithms for GOES-R ABI using MSG SEVIRI as a proxy, *Remote Sens. Environ.*, **115**, 3647–3658

Petrenko, B., A. Ignatov, Y. Kihai, J. Stroup, P. Dash, 2013a: Evaluation and selection of SST regression algorithms for JPSS VIIRS. *Journal of Geophysical Research, submitted.*

Petrenko, B., Y. Kihai, X. Liang and J. Stroup, 2013b: ACSPO v.2.20. Interface control document, NOAA STAR.

Petrenko, B., A. Ignatov, P. Dash, Y. Kihai, X. Liang, 2013c: The ACSPO Clear-Sky Mask (ACSM). *OSI SAF SST Retrieval workshop, 5-7 March 2013, Lannion, France,* http://www.star.nesdis.noaa.gov/sod/sst/xliang/lannion_agenda/presentations/cl_mask/ACSPO_Clear-Sky_Mask_v03.pdf

Pinkley, L.W., P.P. Sethna & D. Williams, 1977: Optical constants of water in the infrared: Influence of temperature. *JOSA*, 678, 494-499.

Prabhakara, C., G. Dalu & V.G. Kunde, 1974: Estimation of SST from remote sensing in the 11-13 μm window region. JGR, 79, 5039-5044

Reynolds, R.W., N.A.Rayner, T.M.Smith, D.C.Stokes, and W. Wang, 2002: An improved in situ and satellite SST analysis for climate, J. Climate, 15, 929-948

Reynolds, R.W., T.M. Smith, C. Liu, C., D.B. Chelton, K.S. Casey, and M.G. Schlax (2007), Daily high-resolution-blended analyses for sea surface temperature, *J. Clim.*, **20**, 5473–5496.R

Reynolds, R.W., N.A. Rayner, T.M. Smith, D.C. Stokes, and W. Wang, 2002: An improved *in situ* and satellite SST analysis for climate. *J. Clim.*, **15**, 1609–1625.

Saunders, P. M., 1967: The temperature at the ocean-air interface. *J. Atmos. Sci.*, **24,** 269-274

Segelstein, D.J., 1981: The complex refractive index of water. M.S. thesis. U. Missouri, Kansas City, MO.

Smith, W.L., R.O. Knuteson, H.E. Revercomb, W. Feltz, H.B. Howell, W.P. Menzel, N.R. Nalli, O. Brown, J. Brown, P. Minnett & W. McKeown, 1996: Observations of the infrared radiative properties of the ocean – implications for the measurement of SST via satellite remote sensing. *BAMS*, 77, 41–51

Stroup, J., ACSPO V2 Principles Document, March 2011

Stuart-Menteth, A.C., I.S. Robinson & P.G. Challenor, 2003: A global study of diurnal warming using satellite-derived SST. *JGR*, 108, 3155, doi:10.1029/2002JC001534

Tanashi, S., H. Kawamura, T. Takahashi & H. Yusa, 2003: Diurnal variations of SST over the wide-ranging ocean using VISSR onboard GMS. *JGR*, 108, 3216, doi:10.1029/2002JC001313

Vazquez-Cuervo, J., E.M. Armstrong & A. Harris, 2004: The effect of aerosols and clouds on the retrieval of infrared SST, *J.Clim.,* 17 (20), 3921–3933

Walton, CC., 1985: Satellite measurement of SST in presence of volcanic aerosols. *J.Clim Appl. Meteor.*, 24, 501-507

Walton, C. C., W. G. Pichel, J. F. Sapper, and D. A. May, 1998: The development and operational application of nonlinear algorithms for the measurement of sea surface temperatures with the NOAA polar-orbiting environmental satellites. *Journal of Geophysical Research*, **103,** 27,999-28,012

Watts, P.D., M.R. Allen & T.J. Nightingale, 1996: Wind speed effects on sea surface emission and reflection for the Along Track Scanning Radiometer. *JTech,* 13, 126-141.

Wick, G., J. Bates & D. Scott, 2002: Satellite and skin-layer effects on the accuracy of SST measurements from the GOES satellites. *JTech*, 19, 1834-1847

Wu, X. & W.L. Smith, 1997: Emissivity of rough sea surface for 8-13 μm: modeling and verification. *Appl.Opt.*, 36, 2609–2619

Xu, F.& A. Ignatov (2010), Evaluation of in situ SSTs for use in the calibration and validation of satellite retrievals, *J. Geoph. Res.*, **115**, *C09022*, doi:10.1029/21010JC006129.

Xu, F. & A. Ignatov (2013), The in situ SST Quality Monitor (*i*Quam), *JTech*, submitted

END OF DOCUMENT